

Phonon Engineering in Hetero- and Nanostructures

Alexander A. Balandin*, Evghenii P. Pokatilov†, and D. L. Nika†

*Nano-Device Laboratory, Department of Electrical Engineering,
University of California – Riverside, Riverside, California 92521, USA*

Phonons, i.e., quanta of lattice vibrations, manifest themselves practically in all electrical, thermal, optical, and noise phenomena in semiconductors and other material systems. Reduction of the size of electronic devices below the acoustic phonon mean free path creates a new situation for the phonons propagation and interaction. From one side, it may complicate heat removal from the down-scaled devices. From the other side, it opens up an opportunity for engineering phonon spectrum in nanostructured materials, and achieving enhanced operation of nanoscale devices. This chapter reviews the development of the nanoscale *phonon engineering* concept and discusses possible device applications. The focus of this review is on tuning the phonon spectrum in the acoustically mismatched nano- and heterostructures in order to change the ability of semiconductors to conduct heat or electric current. New approaches for the electron–phonon scattering rates suppression and improvement of the carrier mobility as well as for formation of the phonon stop-bands are discussed. The phonon engineering concept can be potentially as powerful as the band gap engineering, which led to some ground-breaking developments in the electronics.

Keywords: Phonon Engineering, Nanostructures, Nanophononics, Phonon Transport, Electron–Phonon Interaction, Confined Phonons.

CONTENTS

1. Introduction	140
2. Acoustic Phonon Dispersion in the Acoustically Mismatched Heterostructures	144
2.1. Theoretical Model for Confined Acoustic Phonons	144
2.2. Confined Phonon Dispersion	145
3. Confined Electron–Confined Phonon Scattering Rates in Three-Layered Heterostructures	151
3.1. Confined Electron States	151
3.2. Confined Electron–Confined Acoustic Phonon Interaction	152
3.3. Confined Electron–Confined Phonon Scattering Rates	153
3.4. Comparison of the Scattering Rates and Discussion	154
4. Phonon Distribution in the Acoustically Mismatched Heterostructures	157
4.1. Phonon Distribution in the Embedded Acoustically Hard Thin Films	158
5. Acoustic Phonon Properties of Nanowires with Elastically Dissimilar Barriers	160
5.1. Theoretical Model for the Rectangular Nanowires with Barriers	160
5.2. Theoretical Models for the Cylindrical Nanowires with Barriers	161
5.3. Acoustic Phonon Engineering in Nanowires with Acoustically Dissimilar Barriers	163
6. Enhancement of the Electron Mobility Limited by Optical Phonons	165

6.1. Electron–Optical Phonon Interactions and Electron Mobility in Wurtzite Heterostructures	165
6.2. Electric Field Effect on the Electron Mobility in Wurtzite AlN/GaN/AlN Heterostructures	166
6.3. Electron Mobility Enhancement in AlN/GaN/AlN Heterostructures with InGaN Nanogrooves	167
Acknowledgements	169
References and Notes	170

1. INTRODUCTION

Phonons are quantized modes of vibration occurring in a rigid crystal lattice, such as the atomic lattice of a solid. One can speak of a gas of phonons, which are quasi-particles of the energy $\hbar\omega$ and quasi-momentum $p = \hbar q$ obeying Bose-Einstein statistics.¹ Phonons manifest themselves practically in all properties of materials. For example, acoustic and optical phonons limit electrical conductivity. Optical phonons strongly influence optical properties of semiconductors while acoustic phonons are dominant heat carriers in insulators and technologically important semiconductors. The long-wavelength acoustic phonons give rise to the sound waves in solids, which explains the name *phonon*.

Similar to electrons, one can conveniently characterize the properties of phonons by their dispersion $\omega(q)$, i.e., dependence of the phonon frequency ω on its wave vector q . In bulk semiconductors with g atoms per unit cell,

*Author to whom correspondence should be addressed.

†On leave from: The Department of Theoretical Physics, State University of Moldova, Chisinau, Republic of Moldova.



Alexander A. Balandin received his M.S. degree in Applied Physics and Mathematics from the Moscow Institute of Physics and Technology (MIPT), Russia in 1991. He received his Ph.D. degree in Electrical Engineering from the University of Notre Dame, USA in 1996. He worked as a Research Engineer in the Electrical Engineering Department of the University of California, Los Angeles (UCLA) from 1997 to 1999. In July 1999, he joined the Department of Electrical Engineering of the University of California, Riverside (UCR), where he is a Professor. He leads the Nano-Device Laboratory (NDL), which he organized in 2000, and serves as a Chair of the Materials Science and Engineering (MSE) Program. In 2005 he was a Visiting Professor at Cambridge University, UK. Professor Balandin's research interests are in the area of electronic materials, nanostructures and nanodevices.

Current research topics in his group include phonon engineering at nanoscale, electron and thermal transport in nanostructures, wide band-gap semiconductors and devices, hybrid bio-inorganic nanosystems and electronic noise phenomena. He contributed to the investigation of the flicker noise in GaN-based field-effect transistors, excitonic processes and phonon transport in semiconductor nanostructures. He has authored more than 90 journal publications and ten invited book chapters. He edited books *Noise and Fluctuations Control in Electronic Devices* (2002) and five-volume *Handbook of Semiconductor Nanostructures and Nanodevices* (2006). He chaired SPIE International Conference on Noise in Electronic Devices and Circuits (2005) as well a number of international conference sessions. He is an Editor-in-Chief of the *Journal of Nanoelectronics and Optoelectronics (JNO)*. His research work was recognized by the ONR Young Investigator Award (2002), National Science Foundation CAREER Award (2001), University of California Regents Award (2000), and the Merrill Lynch Innovation Award for "commercially valuable engineering research" (1998). He is a senior member of IEEE, a member of APS, AAAS, SPIE, and Eta Kappa Nu. More information on his research can be found at <http://ndl.ee.ucr.edu/>.



Evghenii P. Pokatilov is Professor at the Department of Theoretical Physics of the State University of Moldova and Doctor of Physics and Mathematics. He has graduated from the State University of Moldova in 1950. He has been working in the State University of Moldova since 1950, holding the following positions: Assistant Professor (1950–1962), Associate Professor (1962–1972), Professor (1972–present), and Head of the Laboratory of Physics of Multi-Layer Structures. He received his Ph.D. degree in Physics and Mathematics from the Institute of Physics and Mathematics of the Ukrainian Academy of Sciences in 1961, and his Doctor of Physics and Mathematics degree from the Institute of Semiconductors, Kiev of the Ukrainian Academy of Sciences in 1972. As a Visiting Scientist or Visiting Professor he worked in the Plovdiv State University, Bulgaria (1975), State University of Antwerp, Belgium (1995–2000 and 2003–2004) and University of California – Riverside,

USA (2001–2003, 2005, and 2007). Professor Pokatilov's research interests are in the area of the polaronic effects, kinetic and optical properties of semiconductors, phonon, electron, hole and exciton states in nanostructures with different size and shapes; thin film, wire and dot superlattices. The current research topics in his laboratory are continuum approximation and dynamic theory of lattice vibrations in the semiconductor quantum dots, quantum wires, and multi-layered planar nanostructures; description of electron, hole and exciton states using the multi-band Hamiltonians. Professor Pokatilov has over 200 technical journal publications, two books and two invited book chapters. In 1987 he received the State Prize, which is the highest award in sciences in Moldova, for his results in the polaron theory, kinetic and optical properties of semiconductors. He has been awarded by the medals Petr Kapitsa (2000) and Akademik Vernadskij (2002) of the Russian Academy of Natural Sciences, Moscow, Russia, and the medal Dumitru Cantemir of Moldovan Academy of Sciences. He graduates 25 Ph.D. students and 3 Doctors of Science. He is a member-correspondent of the Moldovan Academy of Sciences since 1989.



Denis L. Nika received his M.S. degree in Physics from the State University of Moldova, Republic of Moldova, in 2001. He received his Ph.D. degree in Theoretical and Mathematical Physics from the State University of Moldova in 2006. From 2003 he worked in the Laboratory of Physics of Multi-Layer Structures, State University of Moldova, as an Associated Researcher (2003–2004), Researcher (2004–2006), and Senior Researcher (2006–present). He was a Visiting Researcher at the University of Antwerp, Belgium (2004) and in the University of California – Riverside (2005 and 2007). His current research interests include the multi-band theory of the electron, hole, exciton and impurity states in quantum wells, wires and dots; acoustic and optical phonon properties of the multi-layered nanostructures; and the theory of the electron-phonon interactions and kinetic effects in the nano-dimensional heterostructures.

there are $3g$ phonon dispersion modes for every value of q . In the limit of long waves, three modes describe the motion of the unit cell, and form the three acoustic phonon branches. The other $3(g-1)$ modes describe the relative motion of atoms in a unit cell, and form the optical phonon branches. Acoustic phonons have nearly linear dispersion, which can be written as $\omega = V_s q$ (where V_s is the sound velocity). Optical phonons, in general, are nearly dispersion-less for small q values (long-wavelength approximation) and have a small group velocity $V_G = d\omega/dq$.

Spatial confinement of phonons in nanostructures and thin films can strongly affect the phonon dispersion and modify phonon properties such as phonon group velocity, polarization, density of states as well as affect phonon interaction with electrons, point defects, other phonons, etc. Modification of the acoustic phonon dispersion is particularly strong in freestanding thin films or in nanostructures embedded into elastically dissimilar materials. Such modification may turn out to be desirable for some applications while detrimental for others. Thus, nanostructures offer a new way of controlling phonon transport via tuning its dispersion relation, i.e., *phonon engineering*.² The concept of engineering the phonon dispersion in nanostructures has the potential to be as powerful as the concept of the band-gap engineering for electrons, which revolutionized the electronic industry. In this review we describe the modification of the acoustic phonon properties and its influence on the electron–acoustic phonon interactions in hetero- and nanostructures. The discussion also includes optical phonons in heterostructures. Specifically, we show that the modification of the optical phonon spectra, size quantization of the optical quasi-bulk modes and emergence of the interface optical modes strongly affect the electron mobility when it is limited by the polar optical phonons.

The idea of looking at the changes that acoustic phonon spectrum experiences in heterostructures has a rather long history. In 50s, Rytov published a series of theoretical papers³ where he analyzed acoustic vibrations in “artificial thinly-laminated media” (something, which now would be referred to as a superlattice) and described folded phonons in such media. The folded phonons were later observed in quantum well superlattices made of different semiconductors⁴. In 80s and early 90s there have been significant amount of theoretical work done aimed at calculating the confined acoustic phonon–electron scattering rates in freestanding thin films and nanowires. Some notable examples of this work include papers from the research groups of Strosio,⁵ Mitin,⁶ Nishiguchi,⁷ and Bandyopadhyay.⁸ Many of the papers on the subject used the elastic continuum approach for calculating phonon dispersion and adopted solution techniques developed in acoustics and mechanics. The prime motivation was to see if the spatial confinement and quantization of the acoustic phonon modes in freestanding thin films or nanowires

produces noticeable effect on the deformation potential scattering of electrons. The opinions were split about how important the acoustic phonon confinement in the description of electron transport in low-dimensional structures. Some theorists argued that the phonon-confinement induced changes for macroscopic characteristics, such as carrier mobility, are not pronounced.^{7,9} Others have found that the deformation potential scattering can be substantially suppressed for certain electron energies.^{6,8}

The interest to the subject has been renewed when Balandin and Wang¹⁰ pointed out that the confinement-induced changes in the acoustic phonon dispersion may also have an effect on the thermal conductivity. The changes in the phonon group velocity and density of states lead to the alteration of the acoustic phonon relaxation on defects and in three-phonon Umklapp processes^{10,11}. The reduction of the thermal conductivity, being a bad news for the thermal management of downscaled electronic devices, is good news for the thermoelectric devices, which require materials with high electrical conductivity and low thermal conductivity.¹² Further developing the idea, Balandin et al.^{13–16} have theoretically shown that in the thin films or nanostructures embedded in the acoustically “fast” materials (materials with larger sound velocity), the phonon group velocity and thermal conductivity can be enhanced along certain directions (see Fig. 1). A possibility of forming phonon stop-bands in quantum dot superlattices and inhibition of the thermal conductivity, beneficial for thermoelectric applications has also been predicted.¹⁷ As a result, the concept of phonon engineering has been extended to include tuning of the acoustic phonon transport to achieve the desired thermal conductivity of the material. Due to the continuing reduction in the electronic device feature size and increased integration densities, the thermal management at nanoscale gains a particular importance.

More recently, the idea of engineering the phonon–electron scattering rates received a new impetus. It has been demonstrated^{13, 18–22} that the effect of the phonon confinement can be made stronger if one considers a hetero- or nanostructure coated with the elastically dissimilar material. In this case, there appears a strongly non-uniform distribution of the phonons in heterostructure layers. The acoustic hardness of the material is characterized by its acoustic impedance $\eta = \rho V_s$, where ρ is the mass density and V_s is the sound velocity. This effect can be used in the design of the nanoscale transistors, vertical field-effect transistors, alternative-gate dielectric transistors, etc. As the transistor feature size W reduces well below the acoustic phonon mean free path (MFP), which is on the order of 50 nm–200 nm in Si at room temperature, the possibilities for engineering phonon dispersion to improve the carrier and heat transport increase tremendously.

The change in the thermal conductivity of semiconductors due to the phonon confinement bares important consequences for electronic industry in a view of continuous

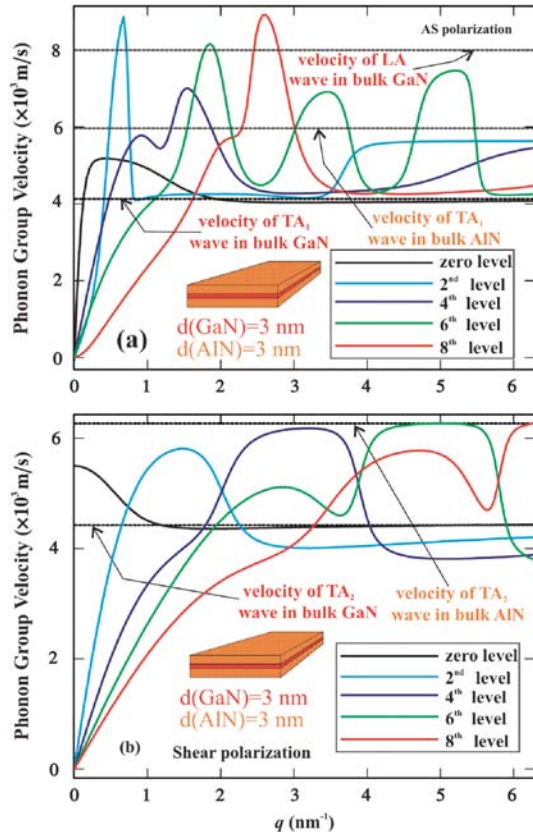


Fig. 1. Phonon group velocity for confined acoustic phonon branches as a function of the phonon wave vector in a three-layered AlN/GaN/AlN heterostructure. The results are shown for (a) AS (flexural) polarization, and for (b) shear polarization. Inset shows the geometry of the heterostructures. Longitudinal and transverse sound velocities in constituent bulk semiconductors are indicated with straight lines. Note in panel (a) and (b) that the phonons in the cladding layer are accelerated compared to bulk owing to the presence of the acoustically hard cladding (barrier) layers.

miniaturization. Heat in technologically important semiconductors is mostly carried by acoustic phonons. The feature size of the state-of-art transistor is already below the room-temperature phonon MFP in Si. In hetero- and nanostructures with feature size W much smaller than the phonon MFP, the acoustic phonon spectrum undergoes strong modification and appears quantized provided the structures are free standing or embedded within material of different elastic properties.^{14, 19} This modification is particularly strong when the structure feature size approaches the scale of the dominant phonon wavelength $\lambda_d \cong 1.48 V_s \hbar / k_B T$. Here k_B is the Boltzmann constant, T is the absolute temperature, and \hbar is the Planck's constant. For many crystalline materials λ_d is on the order of 1.5 nm–2 nm at room temperature, which is about the size of a gate dielectric thickness.

Thermal conductivity in-plane of thin films or along the length of nanowires can decrease for two basic reasons.

The first is the co-called classical size effect on thermal conductivity related to increased phonon–rough boundary scattering.^{23, 24} This effect is pronounced when W is on the order of phonon MFP. It can be observed even in bulk samples at low temperature when the phonon MFP is long. If the structure dimensions $W \ll$ MFP, another effect takes place. Due to flattening of the dispersion branches, the population average phonon group velocity decreases leading to the increased phonon scattering on defects and in Umklapp processes over certain ranges of the phonon energies.^{10–11} Embedding nanostructures into acoustically faster and harder barrier (cladding) layers can lead to the overall increase in the average phonon group velocity. In the described phenomena, the lateral (cross-plane) confinement of acoustic phonon modes in structures with $W \ll$ MFP affect in-plane (along the length) phonon and heat transport.

Recently, Li et al.²⁵ reported on fabrication and measurement of thermal conductivity in single crystalline free-surface Si nanowires with diameters as small as 22 nm. The experimentally observed strong decrease of the thermal conductivity K in such nanowires ($K \sim 9$ W/cm K at $T = 300$ K) was in excellent agreement with the earlier theoretical prediction ($K \sim 13$ W/cm K at $T = 300$ K) of Zou and Balandin,¹¹ which explained the decrease by the acoustic phonon confinement and boundary scattering in Si nanowires.

Spatial confinement of acoustic phonons in nanoscale structures with the large mismatch of the acoustic impedances η , at the boundaries can strongly affect the phonon spectrum and substantially modify the electron–phonon interaction in comparison with bulk. Analyzing the confined phonon dispersion we came to the conclusion that the sound velocity V_s has to be used as an additional parameter (together with the acoustic impedance) to characterize the effects of the boundaries. Thus, in the discussion to follow we will use terminology “acoustically soft” for the material with small η and “acoustically slow” for the material with small V_s . In such structures, both confinement of electron states and acoustic phonons should be taken into account while calculating the scattering rates.

Most recently, Pokatilov et al.^{15–16, 19} have shown theoretically that in heterostructures, such as thin films or nanowires embedded into acoustically slower and softer materials, the drastic modifications of the phonon dispersions take place and the acoustic properties of different layers are hybridized in each of the phonon branches. In all calculated dispersion curves $\omega_s(q)$ there are wide regions of the phonon wave vector q , where the phonon group velocities $d\omega_s(q)/dq$ are close to the bulk velocity in the slower and softer materials. There also exist narrow regions of q , where $d\omega_s(q)/dq$ are close to the bulk velocity in the faster and harder materials. The phonon modes from the wide q regions with the small group velocities practically do not penetrate into the harder and faster

nanostructure layers (the effect, we refer to as phonon depletion in the harder and fast layers). At the same time, the phonon modes from the narrow q regions with the high group velocities are concentrated in the harder and faster materials (the phonon accumulation or localization in the harder and fast layers).

2. ACOUSTIC PHONON DISPERSION IN THE ACOUSTICALLY MISMATCHED HETEROSTRUCTURES

In order to investigate the role of the cladding (barrier) material on the acoustic phonon spectrum of ultra-thin films we consider a free-standing single thin film, e.g., slab, and a free-standing three-layered structure, e.g., double heterostructure. Both structures have a nanometer feature size along the growth direction. A schematic view of the slab and three-layered structure are shown in the insets to Figures 2(a–b). The axis X_1 and axis X_2 in the Cartesian coordinate system are in the plane of the layers while the axis X_3 is directed perpendicular to the layer surfaces. The layer thickness is denoted by d_i ($i = 1, 2, 3$). The structure is symmetric, $d_1 = d_3$, with total thickness $d = 2d_1 + d_2$. As an example system we first consider AlN/GaN/AlN heterostructure. Here we limit our analysis to wurtzite GaN as technologically more important. It is further assumed that the layers have hexagonal symmetry with a crystallographic axis c directed along a coordinate axis X_3 .

2.1. Theoretical Model for Confined Acoustic Phonons

The theoretical model and the calculation procedures described in this section mostly follow the derivation reported in Ref. [14]. The equation of motion for the elastic vibrations in an anisotropic medium can be written as

$$\rho \frac{\partial^2 U_m}{\partial t^2} = \frac{\partial \sigma_{mi}}{\partial x_i} \quad (1)$$

where $\vec{U}(U_1, U_2, U_3)$ is the displacement vector, ρ is the mass density of the material, σ_{mi} is the elastic stress tensor given by, $\sigma_{mi} = c_{mijk} U_{kj}$ and $U_{kj} = \frac{1}{2}((\partial U_k / \partial x_j) + (\partial U_j / \partial x_k))$ is the strain tensor. The normal acoustic vibration modes in multilayered structures have been studied by Rytov³ in homogeneous ($c_{iklm} = \text{const.}$) and isotropic medium approximation by enforcing the boundary conditions on all interfaces of the structures. In this chapter we modify the form of the boundary conditions to make them more convenient for the numerical solution for a multilayered wurtzite heterostructure. When taking derivatives in Eq. (1), one has to take into account that the system is non-uniform along the X_3 axis. The elastic modules are the piece-wise functions of x_3 :

$$c_{mijk} = c_{mijk}(x_3) \quad (2)$$

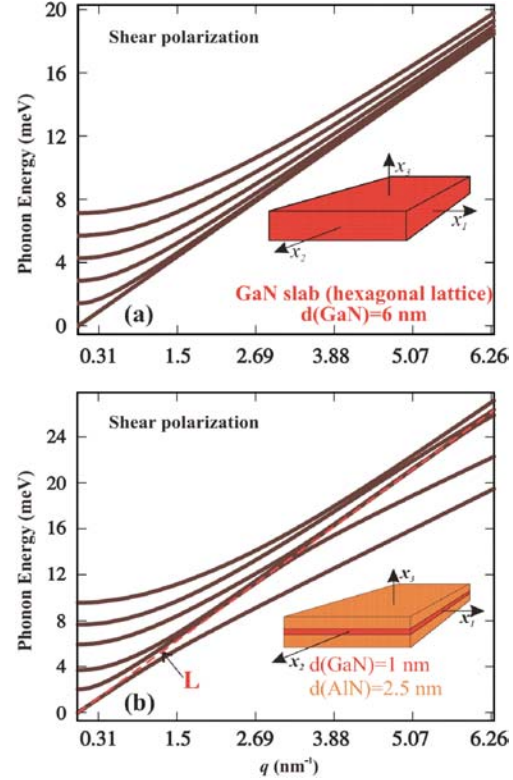


Fig. 2. Phonon energies as the functions of the phonon wave vector for the shear polarization for (a) a 6 nm width semiconductor GaN slab and for (b) a AlN/GaN/AlN three-layered heterostructure with dimensions 2.5 nm/1 nm/2.5 nm. Insets show the slab geometry and coordinate system. Reprinted with permission from [14], E. P. Pokatilov et al., *Superlatt. Microstruct.* 33, 155 (2003). © 2003, Elsevier.

To reduce the number of subscript indexes in the coefficients c_{mijk} , we adopt the two-index notations according to the prescription $1111 \rightarrow 11$; $2222 \rightarrow 22$; $3333 \rightarrow 33$; $1122 \rightarrow 12$; $1133 \rightarrow 13$; $1313 \rightarrow 44$; $2323 \rightarrow 55$; $1212 \rightarrow 66$.

In crystals with hexagonal symmetry the following equalities are valid:

$$c_{1313} = c_{2323} = c_{44}; \quad c_{1212} = c_{66} = (c_{11} - c_{12})/2 \quad (3)$$

Thus, we have five independent elastic constants to characterize the material. An application of the anisotropic continuum model allows us to explicitly include the specifics of lattice structure of wurtzite crystals. The equations of motion obtained in anisotropic medium approximation with such selection of the elastic constants will be completely different from the equations of motion in the isotropic elastic medium approximation or anisotropic medium approximation for cubic crystals.

The axis X_1 is assumed to be along the propagation direction of the acoustic waves. Since the three-layered structure is homogeneous in the plane (X_1, X_2), we look

for the solution of the Eq. (1) in the following form

$$U_i(x_1, x_3, t) = u_i(x_3)e^{i(\omega t - qx_1)} \quad (i = 1, 2, 3) \quad (4)$$

where u_i are the amplitudes of the displacement vector components, ω is the phonon frequency q is the phonon wave vector and i is imaginary unit. A shear polarization, e.g., the displacement vector is parallel to the structure surfaces, can be distinguished from the others using the following definition

$$\rho \frac{\partial^2 U_2}{\partial t^2} = \frac{\partial \sigma_{2i}}{\partial x_i} \quad (5)$$

By substituting Eq. (4) for $i = 2$ to Eq. (5) and taking into account Eqs. (2)–(3), one can turn the partial differential Eq. (5) into an ordinary second order differential equation

$$-\rho\omega^2 u_2(x_3) = c_{44} \frac{d^2 u_2(x_3)}{dx_3^2} + \frac{dc_{44}}{dx_3} \cdot \frac{du_2(x_3)}{dx_3} - c_{66} q^2 u_2(x_3) \quad (6)$$

Derivatives dc_{ik}/dx_3 account for the fact that the structure is heterogeneous. In the case of a slab, one can obtain a simple analytical solution from Eq. (6) by setting $dc_{44}/dx_3 = 0$ (see, for example Refs. [26, 27]). The external surfaces of the three-layered structure are assumed to be free. As a result, the force components along all coordinate axes equal to zero, e.g., $P_1 = P_2 = P_3 = 0$, where $P_i = \sigma_{ik} n_k$, and \vec{n} is the vector normal to the surfaces of the structure $\vec{n} = (0, 0, n_3)$. Thus, on the outer surfaces of the structure the following relationship is satisfied

$$\frac{\partial u_2}{\partial x_3} = 0 \quad (7)$$

For the two other vibrational polarizations ($i = 1, 3$) with the displacement vector components U_1 and $U'_3 = -iU_3$ we obtain the system of two interrelated equations using Eqs. (1) and (4). These equations are given as

$$\begin{aligned} -\rho\omega^2 u_1(x_3) = & -q^2 c_{11} u_1(x_3) + c_{44} \frac{d^2 u_1(x_3)}{dx_3^2} \\ & + q(c_{13} + c_{44}) \frac{du'_3(x_3)}{dx_3} \\ & + \frac{dc_{44}}{dx_3} \left(\frac{du_1(x_3)}{dx_3} + qu'_3(x_3) \right) \end{aligned} \quad (8)$$

$$\begin{aligned} -\rho\omega^2 u'_3(x_3) = & -q^2 c_{44} u'_3(x_3) + c_{33} \frac{d^2 u'_3(x_3)}{dx_3^2} + \frac{dc_{33}}{dx_3} \frac{du'_3(x_3)}{dx_3} \\ & - q \left[(c_{44} + c_{13}) \frac{du_1(x_3)}{dx_3} + \frac{dc_{13}}{dx_3} u_1(x_3) \right] \end{aligned} \quad (9)$$

with the following boundary conditions on the outer surfaces of the structure

$$\frac{du_1}{dx_3} + qu'_3 = 0, \quad -qc_{13}u_1 + c_{33} \frac{du'_3}{dx_3} = 0 \quad (10)$$

Due to the spatial symmetry of the considered three-layered structure and the mathematical form of Eqs. (8)–(9), the displacement vector should have components with an opposite parity, e.g., (u_1^S, u_3^A) or (u_1^A, u_3^S) , where $u_i^S(x_3)$ ($i = 1, 3$) is a symmetrical function of x_3 while $u_i^A(x_3)$ ($i = 1, 3$) is an anti-symmetrical function of x_3 . The upper indexes SA and AS of displacement vectors $\vec{u}^{SA} = \vec{u}(u_1^S, u_3^A)$ and $\vec{u}^{AS} = \vec{u}(u_1^A, u_3^S)$ distinguish independent vibrational polarizations which, together with the shear modes, compose a full set of normal vibrational modes in the structure. In the case of a slab the SA modes are referred to as dilatational modes while AS modes are termed the flexural modes.^{3, 8, 26–27}

2.2. Confined Phonon Dispersion

To obtain the vibrational spectrum, e.g., phonon dispersion, of the three-layered structure we solve the differential Eq. (6) with boundary condition of Eq. (7) for shear polarization, and the system of Eqs. (8)–(9) subject to the boundary conditions of Eq. (10) for SA and AS polarizations. The equations are solved using the finite difference method. The calculations are performed for each value of the phonon wave vector q from the interval $q \in (0, \pi/a)$, where a is the lattice constant in the plane (X_1, X_2) . Since we are interested in the properties of ultra thin films (quantum wells), we assume that the structure is non-relaxed and, thus, the lattice constant is the same for both the thin film and barrier materials. The phonon dispersion is calculated for all three polarizations: shear, SA and AS. Material parameters used in our simulations have been taken from Refs. [28–31].

The characteristic features of the phonon dispersion relations can be easily seen on the plots of the phonon group velocity as a function of the wave vector q , which is given as

$$v_s^{SA, AS, sh}(q) = \frac{d}{dq} \omega_s^{SA, AS, sh}(q) \quad (11)$$

Here the superscript denotes the polarization type, while the subscript s is the quantum number of the modes with a given polarization. Using the above expression we then calculate the group velocity for each mode.

First, we consider phonon modes of the shear polarization, for which the effects of quantization and the system heterogeneity are exhibited in more pronounced way than those for SA and AS polarizations. Figures 2(a, b) and 3(a, b) show the dispersion relation $\hbar\omega_s^{sh}(q)$ and the group velocity $v_s^{sh}(q)$ for a set of shear modes. Figure 2(a) and Figure 3(a) present data for a GaN slab with thickness $d = 6$ nm. Figures 2(b) and 3(b) present data for a three-layered AlN/GaN/AlN with dimensions 2.5 nm/1 nm/2.5 nm. For convenience of the further discussion, we refer to such heterostructure as a type-I structure to emphasize that the cladding layers are thicker than the core layer. One can see

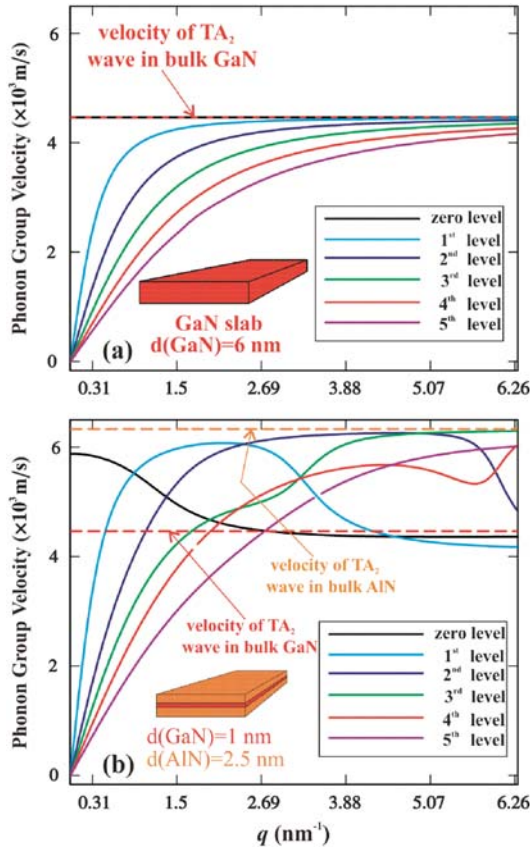


Fig. 3. Phonon group velocities as the functions of the phonon wave vector for the shear polarization. Results are shown for (a) a 6 nm wide semiconductor GaN slab and for (b) a AlN/GaN/AlN three-layered heterostructure with dimensions 2.5 nm/1 nm/2.5 nm. Reprinted with permission from [14], E. P. Pokatilov et al., *Superlatt. Microstruct.* 33, 155 (2003). © 2003, Elsevier.

from Figure 2 that near the Brillouin zone center (small values of q) the phonon modes are quantized and the modes with $s \neq 0$ are quadratically dispersive. In the zone center the phonon group velocity is a liner function of the phonon wave vector $v_s^{\text{sh}}(q) = a_s q$ (see Fig. 3(a)).

With increasing q all dispersion curves approach a limit $\hbar\omega_0(q) = v_0 \hbar q$, where $v_0 = v^{\text{TA}_2}(\text{GaN})$ and $v^{\text{TA}_2}(\text{AlN})$ is the velocity of the transverse acoustic wave propagating along X_1 axis and polarized along X_2 axis (TA_2 polarized waves). The mode with $s = 0$ is bulk-like for all values of q . For large values of q (see Figs. 2(a–b)) modes with $s \neq 0$ also become GaN bulk-like. Note, that in the case of the clamped surface boundary conditions (which can be obtained in the limit of the claddings with the infinite hardness only) the zero bulk-like mode vanishes. The strong size-quantization of the phonon spectra for the small values of q , emergence of quasi-optical modes and significant decrease of the phonon group velocity ($v_s(q) < v^{\text{TA}_2}(\text{GaN})$) constitute the phonon confinement effects in an ultra-thin slab. These effects were shown to have a

pronounce influence on the lattice (phonon) thermal conductivity of semiconductor quantum wells.¹⁰

The inhomogeneity of the three-layered structure changes the shape of the dispersion curves both quantitatively and qualitatively (compare panels (a) and (b) in Figs. 2 and 3). The steep segments of each of the dispersion curves in Figure 2(b) distinguish these curves from the monotonic dispersion curves of Figure 2(a). These segments are arranged in order of increasing mode number s and can be joined together by a straight line, which is indicated in Figure 2(b) by the symbol “L”. One can also define a characteristic velocity as $\hbar\omega_L(q) = v_L \hbar q$. As one can see from Figure 3(b), the phonon group velocities on these segments coincide approximately with the velocities of TA_2 bulk phonons in AlN. Thus, on a straight line L the phonon modes are (AlN, TA_2) bulk-like.

The dispersion curves to the left and above the line L appear to look like dispersion curves in a slab. This region of strong phonon size-quantization is qualitatively similar for all considered structures and polarizations. The modes with small s and large phonon wave vector q split off down from line L and are (GaN, TA_2) bulk-type. For large s at large q the phonon modes are (AlN, TA_2) bulk-type (see Fig. 3(b)). The phonon modes in the multi-layered structure are formed as result of superposition of vibrations from different layers on the structure interfaces, which leads to the mode hybridization. It is interesting to note, that depending on the q value the hybrid modes can reveal signatures of the specific layers signatures rather than those of the averaged structure properties. For example, the group velocity for the mode with $s = 1$ at moderate q is $v^{\text{TA}_2}(\text{AlN})$, while at large q the group velocity is $v^{\text{TA}_2}(\text{GaN})$, although the total width of the cladding AlN layers is five times larger than the width of the core GaN layer. The group velocity of the mode $s = 5$ tends monotonically to the bulk velocity $v^{\text{TA}_2}(\text{AlN})$. Figure 4 illustrates “retraction” of the mode $s = 0$ to the acoustically slow core GaN layer from the acoustically fast AlN cladding layer as the phonon wave vector q increases. As a result the group velocity of this mode changes from $v = v^{\text{TA}_2}(\text{AlN})$ at small q to $v = v^{\text{TA}_2}(\text{GaN})$ for large q .

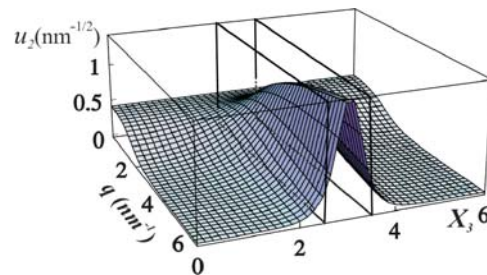


Fig. 4. Dependence of the normalized amplitude $u_2(x_3)$ on the wave vector k in the type-I heterostructure. Outer parallelepipeds correspond to AlN cladding layers while interior parallelepiped corresponds to GaN core layer. Reprinted with permission from [14], E. P. Pokatilov et al., *Superlatt. Microstruct.* 33, 155 (2003). © 2003, Elsevier.

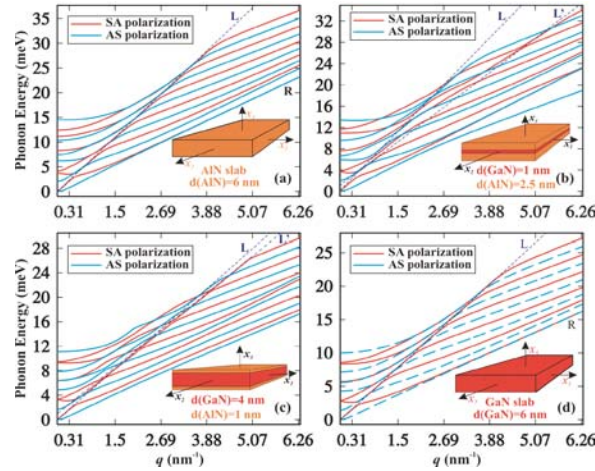


Fig. 5. Energy dispersion of the SA and AS acoustic phonon modes. The results are shown for (a) the 6 nm width AIN slab and (b) the heterostructure type I with the cladding layer thickness $d_1 = d_3 = 2.5$ nm and the core layer thickness $d_2 = 1.0$ nm; as well as for (c) the heterostructure type II with the cladding layer thickness $d_1 = d_3 = 1.0$ nm and the core layer thickness $d_2 = 4.0$ nm and (d) the 6 nm width GaN slab. Inset shows the geometry of the slab and three-layered structure. Reprinted with permission from [14], E. P. Pokatilov et al., *Superlatt. Microstruct.* 33, 155 (2003). © 2003, Elsevier.

In Figures 5(a–d) and 6(a–d) we present the evolution of the phonon dispersion and group velocity for SA (red line) and AS (blue line) modes in a three-layered structure when core layer width increases from 0 nm (AIN slab (Figs. 5(a), 6(a))) to 6 nm (GaN slab (Figs. 5(d), 6(d))). One can notice in Figs. 5(a, d) that the characteristic line L can be identified for the slab SA and AS modes whereas it is absent for the shear slab modes shown in Figure 2(a). The slope v_L of the line L is approximately equal to v^{LA} (AIN), where v^{LA} is the velocity of the longitudinal acoustic wave propagating along X_1 (LA polarized waves). In the limit of large phonon wave vectors q , the group velocity is the same for almost all modes. Its value is slightly lower than the bulk transverse sound velocity v^{TA_1} (AIN) (see Fig. 5(a)) and v^{TA_1} (GaN) (see Fig. 5(d)) due to the phonon confinement or “slab” effect. Here v^{TA_1} is the velocity of the transverse acoustic wave propagating along X_1 axis and polarized along the reference axis (TA_1 polarized waves). The appearance of line L in the phonon energy dispersion for a simple slab is explained by mixing of waves with potential and solenoidal polarizations (LA and TA_1 polarizations in a bulk limit).

Figure 5(c) presents results for the structure, which we refer to as structure type-II to identify that it consists of a “thick” core layer and “thin” cladding layers. In the tree-layered heterostructures of type-I and type-II one can spot two characteristic lines (L and L') shown in Figures 5(b, c)). Correspondingly, the group velocity curves in Figures 6(b, c) display two different maxima. The sequence of the higher maxima corresponds to the

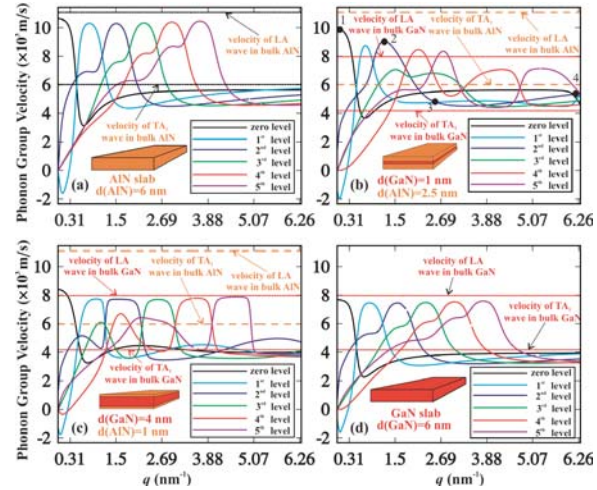


Fig. 6. Phonon group velocities as the functions of the phonon wave vector for the SA acoustic phonon modes. The sizes of the slabs (a, d) and heterostructures (b, c) are same as in the previous Figures 3(a–d). Reprinted with permission from [14], E. P. Pokatilov et al., *Superlatt. Microstruct.* 33, 155 (2003). © 2003, Elsevier.

line L with the slope $v_L \approx v^{LA}$ (AIN) while the sequence of the lower maxima corresponds to the line L' with the slope $v_{L'} \approx v^{LA}$ (GaN). The existence of two lines (L and L') in the phonon energy spectra is a result of waves mixing and hybridization in the heterostructure. Both lines are clearly seen in Figure 5(b) for the type-I heterostructure while for the type-II heterostructure (Fig. 5(c)) the line L is defined by the initial segment of the mode $s = 0$ curve only. The reduction of the AIN-like modes in type-II heterostructure is explained by a much thicker GaN core layer, which leads to the decrease of the group velocities of all phonon modes. The lines L and L' divide the phonon dispersion into three distinctively different regions (see Figs. 5(b, c)): (i) region of the strong phonon size quantization for small q and to the left from line L; (ii) region with abrupt change of dispersion characteristics between lines L and L', and (iii) region to the right from line L' with low-frequency modes and with group velocities approaching the low bulk velocity v^{TA_1} (AIN) (see Fig. 5(b)) and v^{TA_1} (GaN) (see Fig. 5(c)). One can notice that AS and SA modes display more the individual layer properties rather than the averaged properties of the heterostructure. Although the narrow region between lines L and L' can be thought of as the one having properties, which are average of the core and cladding layer properties. Another observation is that the Rayleigh line (R) (Ref. [3]), which is present in Figures 5(a, d) for simple slabs does not appear in the heterostructure energy spectra (Figs. 5(b, c)).

The behavior of the phonon dispersion and group velocity is determined by the specifics of the distribution of the displacement vectors in the layers of the heterostructure. As an example, in Figures 7(a–d) we show the components of the displacement vectors $u_{1,s}^{SA}(x_3)$ (blue line) and

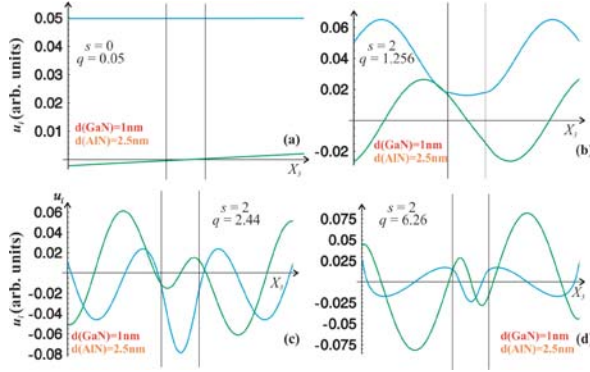


Fig. 7. Components of the displacement vector u_1 (solid line) and u_3 (dashed line) of SA phonon modes as the functions of the coordinate x_3 . The results are shown for four phonon modes: (a) $n = 0$, $k = 0.05 \text{ nm}^{-1}$; (b) $n = 2$, $k = 1.256 \text{ nm}^{-1}$; (c) $n = 2$, $k = 2.44 \text{ nm}^{-1}$; (d) $n = 2$, $k = 6.26 \text{ nm}^{-1}$. Reprinted with permission from [14], E. P. Pokatilov et al., *Superlatt. Microstruct.* 33, 155 (2003). © 2003, Elsevier.

$u_{3,s}^{\text{SA}}(x_3)$ (green line) for the type-I structure. The chosen modes s and values of the phonon wave vector q are the following: $s = 0$, $q = 0.05 \text{ nm}^{-1}$ (a); $s = 2$, $q = 1.256 \text{ nm}^{-1}$ (b); $s = 2$, $q = 1.44 \text{ nm}^{-1}$ (c); and $s = 2$, $q = 6.28 \text{ nm}^{-1}$ (d). These four cases (a–d) shown in Figure 7 correspond to the points on the group velocity plot in Figure 6(b) indicated by filled circles. One can see from Figure 7(a) that the amplitude $u_{1,s=0}^{\text{SA}}(x_3)$ is constant in all layers of the heterostructure. The latter together with the fact that the combined thickness of the cladding layers is much larger than the thickness of the core layer explain the (AlN, LA)-like nature of this mode. The mode $s = 2$ at $q = 1.256 \text{ nm}^{-1}$ (see Fig. 7(b)) is also (AlN, LA)-like since the amplitude $u_{1,s=2}^{\text{SA}}(x_3)$ is distributed predominantly in the cladding layer. The contributions of different polarizations, e.g., potential, solenoidal, to the displacement vector \vec{U} can be obtained by calculating $\text{div } \vec{U}$ and $\text{curl } \vec{U}$. Such calculation for mode $s = 0$ at $q = 0.05 \text{ nm}^{-1}$ demonstrates that this mode is LA bulk-like, which is in complete agreement with Figure 5(b)) since $\text{curl } \vec{U} = 0$ and $\text{div } \vec{U} \neq 0$ for this case.

For calculation of different macroscopic characteristics of nanostructures, such as thermal and electrical conductivity, heat capacity, etc., it is required to know the spectral density of the phonon mode distribution, e.g., phonon density of states. In the considered plane structures with thin core and cladding layers the phonon wave vector is two-dimensional. Thus, the phonon density of states for each of the SA, AS or shear polarizations with given mode number s is defined by the expression

$$f_s^{\text{SA, AS, sh}}(\omega) = \frac{1}{2\pi} q_s^{\text{SA, AS, sh}}(\omega) \frac{dq_s^{\text{SA, AS, sh}}(\omega)}{d\omega} \quad (12)$$

The total phonon density of states for all polarizations is obtained by a summation over all s

$$F^{\text{SA, AS, sh}}(\omega) = \sum_s f_s^{\text{SA, AS, sh}}(\omega) \quad (13)$$

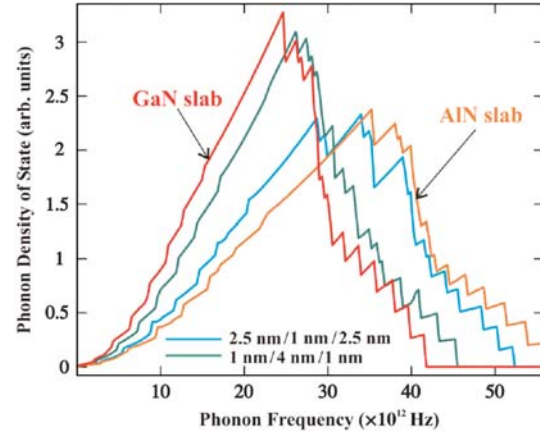


Fig. 8. Total phonon density of states as the function of the phonon frequency for the GaN slab, for the AlN slab and for type I and type II heterostructures. The structures sizes are shown in the figure. Reprinted with permission from [14], E. P. Pokatilov et al., *Superlatt. Microstruct.* 33, 155 (2003). © 2003, Elsevier.

For the type-I and type-II three-layered structures the total phonon density of states $F^{\text{SA, AS, sh}}(\omega)$ is presented in Figure 8. For comparison, the total phonon density of states in simple GaN and AlN slabs is also shown. The oscillatory behavior of the density of states functions in the three-layered structure for each polarization is a manifestation of the phonon mode quantization and their *quasi*-optical nature ($\omega(q = 0) \neq 0$). Local steps in the density of states correspond to the onsets of new phonon branches when their cut-off frequencies are reached. Altering the phonon density of states in the three-layered structure for low frequencies can lead to the significant change in the electron–phonon scattering rates particularly for low temperatures.

The average phonon group velocity is an important characteristic that determines, for example, the lattice thermal conductivity of bulk semiconductors or nanostructures.^{10, 11} We calculate the average phonon group velocity for each polarization as a velocity of a wave packet with the modes populated in accordance with the Bose-Einstein distribution function

$$\bar{v}^{\text{SA, AS, sh}}(T) = \frac{\int_{\omega_{\min}}^{\omega_{\max}} d\omega n(\frac{\hbar\omega}{T}) \sum_s v_s^{\text{SA, AS, sh}}(\omega) f_s^{\text{SA, AS, sh}}(\omega)}{\int_{\omega_{\min}}^{\omega_{\max}} d\omega n(\frac{\hbar\omega}{T}) \sum_s f_s^{\text{SA, AS, sh}}(\omega)} \quad (14)$$

where $n(\hbar\omega/T)$ is the Bose-Einstein equilibrium distribution function for phonons. Figure 9 shows the average phonon group velocity $\bar{v}^{\text{SA, AS, sh}}(T)$. The results are presented for all three phonon polarizations: SA (red line), AS (blue line), and shear (green line). In type I and type II heterostructures, the average velocity of the thermal phonon current is considerably higher than that in the GaN slab, which is explained by the influence of the AlN cladding. For example, in the type-I structure at $T = 300 \text{ K}$ the following ratios for the group velocities were found

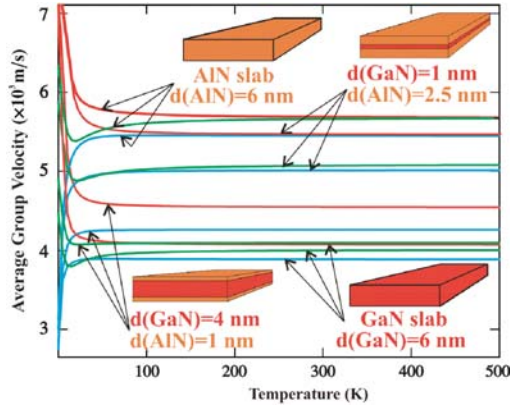


Fig. 9. Population averaged phonon group velocities as the functions of temperature for the AlN, GaN slabs and type I and type II heterostructures. The results are shown for SA (solid line), AS (dotted line), and shear (dashed line) phonon polarizations. Reprinted with permission from [14], E. P. Pokatilov et al., *Superlatt. Microstruct.* 33, 155 (2003). © 2003, Elsevier.

$$v^{SA}(\text{type-I})/v^{SA}(\text{GaN}) = 1.35, v^{AS}(\text{type-I})/v^{AS}(\text{GaN}) = 1.29, \text{ and } v^{sh}(\text{type-I})/v^{sh}(\text{GaN}) = 1.26.$$

Our results demonstrate that it is possible to tune the velocity of the phonon flux in a semiconductor quantum well layer over a wide range of value. By proper selection of the material and width of the cladding layers one can either considerably increase or decrease the phonon group velocity in the core quantum well layer. This is an important capability for heat transport. Indeed, thermal conductivity coefficient K_T can be approximately written as $K_T \sim C_V V \Lambda$ where C_V is the specific heat per unit volume, Λ is the average phonon mean free path, and $V = \Sigma \bar{v}^{SA, AS, sh}$ is the phonon group velocity averaged over all polarizations and directions. For small wave vectors in bulk material this velocity coincides with the sound velocity. Thus, the thermal conductivity coefficient depends on the phonon velocity implicitly and through the phonon mean free path Λ , which is a strong function of the phonon group velocity. In the next subsection we examine the range over which the group velocity can be changed by combining the acoustically fast and acoustically slow materials.

In order to demonstrate a possibility of strong modification of the phonon group velocity and, correspondingly the heat current in confined structures, by choosing cladding layers, we consider two new structures. Structure type-III is a GaN layer embedded in some acoustically slow and soft plastic material: plastic/GaN/plastic. We consider that GaN layer is very thin, on the order of 1 nm, so that it can be considered as a quantum well. The chemical structure of the plastic material used for the cladding layers is not essential for our analysis. We only assume that the sound velocity in bulk plastic is 2000 m/s, and mass density is 1 g/sm³. The chosen values of these parameters correspond to those of a large number of materials used in practice.³² Another structure under consideration, type-IV,

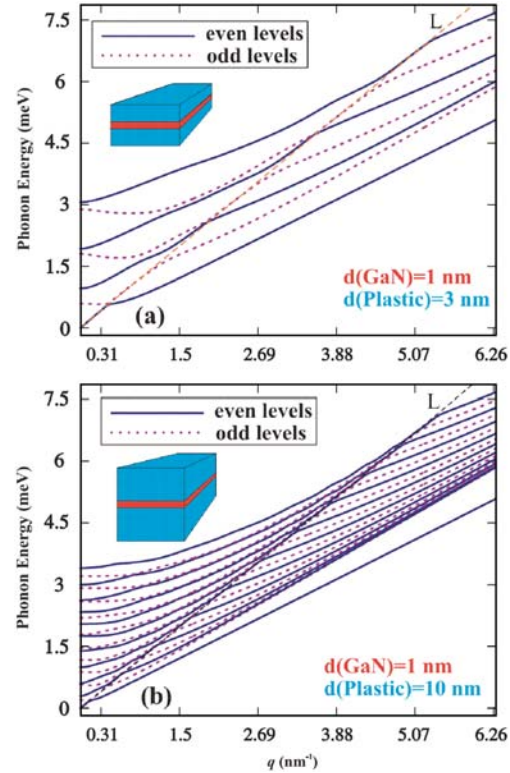


Fig. 10. Energy dispersion of the SA acoustic phonon modes for type III heterostructures. The results are shown for (a) the heterostructure with the cladding layer thickness $d_1 = d_3 = 3.0$ nm and the core layer thickness $d_2 = 1.0$ nm; as well as for (b) the heterostructure the cladding layer thickness $d_1 = d_3 = 10.0$ nm and the core layer thickness $d_2 = 1.0$ nm. Reprinted with permission from [14], E. P. Pokatilov et al., *Superlatt. Microstruct.* 33, 155 (2003). © 2003, Elsevier.

consists of a very thin layer of plastic embedded within two layers of the acoustically fast material such as sapphire: $\text{Al}_2\text{O}_3/\text{plastic}/\text{Al}_2\text{O}_3$. We carry out simulations for these two new structures following the procedure outlines above.

In Figures 10(a–b) and 11(a–b) we show the dispersion relations $\hbar\omega(k)$ for SA modes in the structure type-III (the thickness of the core GaN layer is fixed at 1 nm while the thickness of each of the two cladding layers spans the values 3 nm and 10 nm) and in structure type-IV (the thickness of the core plastic layer is fixed at 1 nm while the thickness of the Al_2O_3 cladding layers spans the values 3 nm and 10 nm). In Figure 10(a) the slope of the line L is approximately equal to the velocity of LA phonons in plastic $v_L \approx v^{LA}(\text{PI})$ while the slope of the dispersion branches $\hbar\omega^{SA}(q)$ to the right from this line approaches TA phonon velocity in plastic $v^{TA}(\text{PI})$. The GaN core contribution is suppressed in this type of structure since the plastic cladding effect and the slab-like phonon confinement effect both lead to the same dispersion flattening. Therefore the type-III heterostructure becomes effectively plastic slab-like. The acoustically slow cladding of the GaN thin films

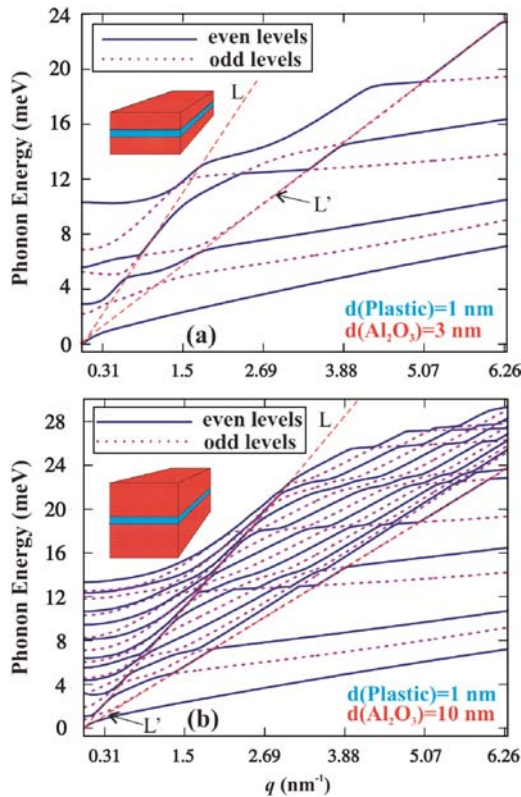


Fig. 11. Energy dispersion of the SA acoustic phonon modes for type IV heterostructures. The results are shown for (a) the heterostructure with the cladding layer thickness $d_1 = d_3 = 3.0$ nm and the core layer thickness $d_2 = 1.0$ nm; as well as for (b) the heterostructure the cladding layer thickness $d_1 = d_3 = 10.0$ nm and the core layer thickness $d_2 = 1.0$ nm. Reprinted with permission from [14], E. P. Pokatilov et al., *Superlatt. Microstruct.* 33, 155 (2003). © 2003, Elsevier.

results in strong phonon deceleration in such structure. The increase of the width of the plastic cladding does not change much in this picture.

Figures 11(a–b) demonstrates the accelerating action of Al_2O_3 claddings on phonon velocity in type-IV heterostructure with the plastic core layer of the thickness $d = 1$ nm. In this case, the phonon confinement “slab effect” and the influence of the Al_2O_3 cladding act in opposite directions and the inhomogeneous nature of heterostructure is strongly manifested. The type-IV heterostructure does not become slab-like even with very thick Al_2O_3 cladding layers. In Figure 11(b) one can see both characteristic lines (L and L') with the slope equal to $v^{\text{LA}}(\text{Al}_2\text{O}_3)$ and $v^{\text{TA}_1}(\text{Al}_2\text{O}_3)$, correspondingly. An intermediate region between these lines is characterized by abrupt and multiple changes in phonon velocity in the interval of values ($v^{\text{TA}}(\text{PI})$, $v^{\text{LA}}(\text{Al}_2\text{O}_3)$). To the right from line L' there is a region of low-velocity phonons ((plastic, TA)-like modes). With increasing width of the cladding layers the intermediate region extends and the number of the “fast” phonon modes increases. At the same time, the

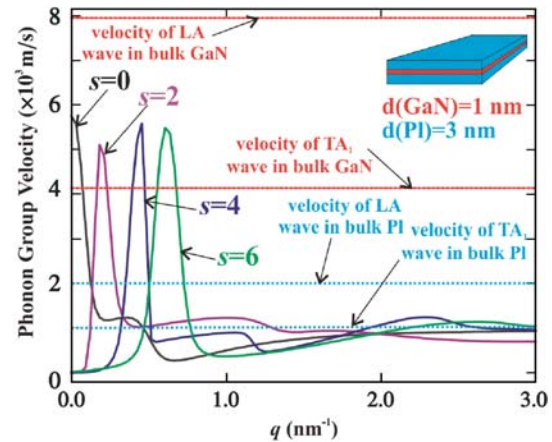


Fig. 12. Phonon group velocity for confined acoustic phonon branches as a function of the phonon wave vector in a three-layered Plastic/GaN/Plastic heterostructure. The results are shown for AS polarization. Longitudinal and transverse sound velocities in constituent bulk semiconductors are indicated with straight lines.

acoustically fast cladding layers do not completely overcome the “slowness” of the core layer. Therefore, the effect of the phonon acceleration in type-IV heterostructure is weaker than the effect of deceleration in type-III heterostructure. The effect of the phonon deceleration in type-III heterostructure (3 nm/1 nm/3 nm) is illustrated in Figure 12 for the phonon branches $s = 0, 2, 4$, and 6. One can see from this figure that in the wide interval of q the phonon velocity in this heterostructure is close to the bulk PI velocity and considerably smaller than the velocities of GaN-slab or bulk.

It is also interesting to compare the averaged phonon group velocity in the three-layered heterostructures and in the corresponding bulk material. For example, in the type-IV structures, the average velocity of the thermal phonon current in the core layer can be made higher than that in the corresponding bulk material. Such velocity increase is due to the influence of the acoustically fast and “thick” cladding layer. In the type II structure (“thin” cladding layer, “thick” core layer) the average velocity in the core GaN layer is lower than that in the bulk GaN. The latter is due to the fact that effect of the barrier here is less pronounced and the velocity change in the core GaN layer is mostly defined by the phonon mode quantization and flattening of the polarization branches (see Figs. 2–3). This is in line with the prediction of the significant decrease of the phonon group velocity in free-standing quantum wells (or slabs)¹⁰ and nanowires.¹¹ We can also conclude that the velocity of the “core-like” phonons in the heterostructure with the fast (slow) claddings also increases (decreases) in comparison with the slab.

In the summary for this section, it has been shown that by proper selection of the cladding material parameters and its thickness, one can make the group velocity in the core layer of such heterostructures either larger or

smaller than in corresponding slab and bulk. For example, it was demonstrated that in a structure that consists of a 1 nm thick GaN core layer embedded into 2.5 nm thick AlN cladding layers, the population averaged phonon group velocity at 300 K is about 30% higher than in GaN slab. The fact that phonon group velocity in heterostructures can be modulated bears important consequences for phonon heat transport and thermal management of electronic devices.

3. CONFINED ELECTRON-CONFINED PHONON SCATTERING RATES IN THREE-LAYERED HETEROSTRUCTURES

In this section we describe the specifics of the confined electron-confined phonon scattering rates on the example of GaN slabs with $d = (2 \text{ nm}, 10 \text{ nm})$ and the three-layered AlN/GaN/AlN heterostructures with dimensions $(4 \text{ nm}/2 \text{ nm}/4 \text{ nm})$ and $(2 \text{ nm}/6 \text{ nm}/2 \text{ nm})$. For convenience of further discussion, we refer to such heterostructures as type A (“thick” barrier–“thin” core) and type B (“thin” barrier–“thick” core) heterostructures, respectively. Details of the calculation of normal phonon modes in AlN/GaN/AlN heterostructures are described in Section 2 of this review. The normal modes with displacement vector \vec{U} parallel to the layers do not interact with charge carriers. Therefore, only two types of normal modes of SA and AS polarization interact with charge carriers. The displacement vectors \vec{U} for SA and AS modes lie in the (X_3, \vec{q}) plane, where \vec{q} is a wavevector of normal vibration. The dispersion relations for type A heterostructure are shown in Figure 13 for both SA (a) and AS (b) polarizations. One can see from these figures that only zero SA mode and zero AS mode are bulk-like. All the other modes are quantized and quasi-optic in nature, e.g., $\omega(q=0) \neq 0$.

3.1. Confined Electron States

We limit our consideration to wurtzite GaN and AlN compounds. Since wurtzite lattice lacks inversion symmetry, the heterostructure layers are spontaneously polarized. The vector of spontaneous polarization P^{sp} is oriented along the c axis. Due to the lattice constant a mismatch, $a(\text{GaN}) > a(\text{AlN})$ by 2.5%, in the type A heterostructure the core GaN layer is uniformly squeezed in the plane (X_1, X_2) , while in the type B heterostructure the cladding AlN layers are stretched in the same plane. As shown in Refs. [33–35] such deformation does not relax for the layer thickness $d(\text{GaN}, \text{AlN}) < 3 \text{ nm}$ and induces polarization P^{st} . The total polarization includes two components, e.g., $P^{\text{tot}} = P^{\text{sp}} + P^{\text{st}}$. If the GaN core layer is relaxed (not under strain) then $P^{\text{tot}} = P^{\text{sp}}$. Theoretical estimates for the built-in electrostatic field F induced by total polarization P^{tot} give the value of about 10^6 V/cm .^{36–37}

The Schrödinger equation for the transverse electron motion in the considered three-layered heterostructure can

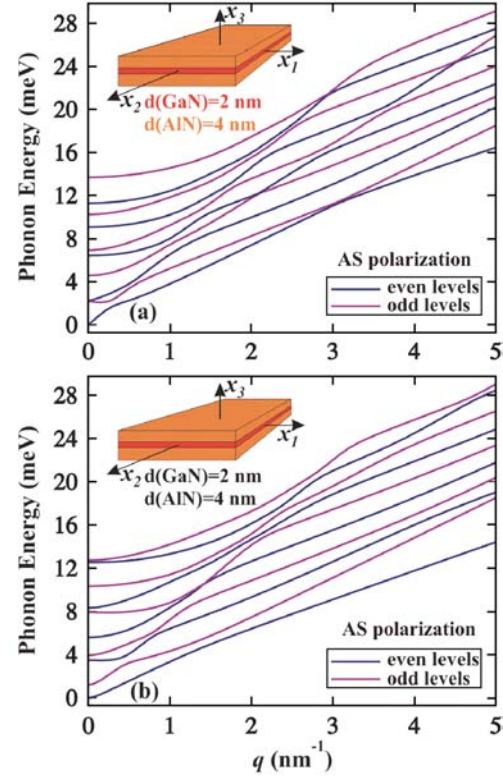


Fig. 13. Phonon energy as the function of the phonon wave vector for type A (“thick” barrier – “thin” core) heterostructure plotted for (a) SA and (b) AS polarizations. Reprinted with permission from [20], E. P. Pokatilov et al., *J. Appl. Phys.* 95, 5626 (2004). © 2004, American Institute of Physics.

be written as

$$\left(-\frac{\hbar^2}{2} \frac{\partial}{\partial x_3} \frac{1}{m_{\parallel}(x_3)} \frac{\partial}{\partial x_3} + V_b(x_3) + V_{\text{build-in}}(x_3) \right) \psi_n(x_3) = \varepsilon_{\perp n} \psi_n(x_3) \quad (15)$$

$$\varepsilon_{\perp n} = E_{\perp n} - \frac{\hbar^2 k^2}{2} \frac{1}{m_{\perp, n}} \quad (16)$$

$$\frac{1}{m_{\perp, n}} = \int_{-\frac{d}{2}}^{\frac{d}{2}} |\psi_n(x_3)|^2 \frac{1}{m_{\perp}(x_3)} dx_3 \quad (17)$$

Here \hbar is the Planck’s constant, $m_{\parallel}(x_3)$ is the effective mass of an electron along the reference axis c and $m_{\perp}(x_3)$ is the effective mass of an electron in the (X_1, X_2) -plane, $V_b(x_3)$ is the barrier potential and $V_{\text{build-in}}(x_3) = -eF_3^w x_3$, where e is the electron charge, F_3^w is the component of the built-in electrostatic field along X_3 axis in the quantum well. Eq. (16) determines the energy of electron level with quantum number n , ψ_n is the wave function of the electron state with a quantum number n .

In Figure 14 the flat band ($V_{\text{build-in}} = 0$; FB) potential well is depicted by the violet line while the triangular potential well (TB), which corresponds to the built-in

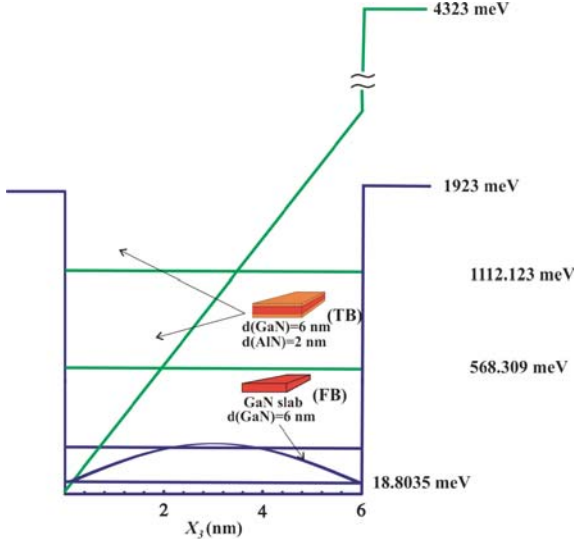


Fig. 14. Electron energy levels and electron wave functions (the ground state and the first excited states) calculated for the potential well without built-in electric potential, e.g., flat-band (FB), indicated by the solid lines, and for the potential well with the built-in electric field, e.g., tilted band (TB) indicated by the dashed lines. Reprinted with permission from [20], E. P. Pokatilov et al., *J. Appl. Phys.* 95, 5626 (2004). © 2004, American Institute of Physics.

electric field intensity $F_3^w = 4$ MV/cm, is shown by the green line. This value of the built-in field, chosen for numeric calculations, has been adopted from Ref. [38]. The energy levels (bottom of the corresponding subband) for the ground and first excited subbands in the FB and TB wells are presented in Figure 14 with the violet and green lines, respectively. One can see that in the case of FB the wave function $\psi_{n=1}(x_3)$ is distributed uniformly over the layer thickness while in the case of TB the wave function $\psi_{n=1}(x_3)$ becomes strongly asymmetric and attains its maximum approximately in the distance equal to one third of the core layer thickness from the interface. This feature of the wave function results in substantial modification of the confined electron–confined phonon interaction in the case of TB as compared with the case of FB.

3.2. Confined Electron–Confined Acoustic Phonon Interaction

In this section we describe the derivation of the Hamiltonian for the confined electron–confined phonon interaction in a three-layered piezoelectric heterostructure following Ref. [20]. The expansion of the displacement vector over the normal modes has the form

$$\vec{U}(x_1, x_2, x_3) = \sum_{\alpha, s} \vec{U}_s^{(\alpha)}(\vec{r}, x_3, \vec{q}), \vec{r}(x_1, x_2) \quad (18)$$

where index $\alpha = (\text{SA}, \text{AS})$ indicates the polarization type and index $s = 0, 1, 2, \dots, N$ is the quantum number of a normal phonon mode. The displacement vector for the

(α, s, \vec{q}) -normal mode is given by the equation

$$\vec{U}_s^{(\alpha)}(\vec{r}, x_3, \vec{q}) = \frac{1}{\sqrt{L_1 L_2}} A_s^{(\alpha)}(\vec{q}, t) \vec{w}_s^{(\alpha)}(\vec{q}, x_3) e^{i\vec{q}\vec{r}} \quad (19)$$

where $A_s^{(\alpha)}$ is the oscillation amplitude and $\vec{w}_s^{(\alpha)}(\vec{q}, x_3)$ is the polarization vector for the (α, s, \vec{q}) -normal mode. The polarization vector $\vec{w}_s^{(\alpha)}(\vec{q}, x_3)$ in its turn satisfies the following orthonormal conditions

$$\int_{-\frac{d}{2}}^{\frac{d}{2}} \vec{w}_s^{(\alpha)}(\vec{q}, x_3) \rho(x_3) \vec{w}_{s'}^{(\alpha')*}(\vec{q}, x_3) dx_3 = \tilde{\rho}_s^{(\alpha)}(\vec{q}) \delta_{ss'} \delta_{\alpha\alpha'} \quad (20)$$

where $\delta_{kk'} = 0 (k \neq k')$ and $\delta_{kk'} = 1 (k = k')$.

The Hamiltonians for interaction of an electron with (α, s, \vec{q}) normal acoustic phonon mode via the deformation potential $\hat{H}_{e-\text{ph}, s}^{(\alpha), d}$, piezoelectric potential $\hat{H}_{e-\text{ph}, s}^{(\alpha), p}$ and ripple potential $\hat{H}_{e-\text{ph}, s}^{(\alpha), \text{rip}}$ are given as

$$\begin{aligned} \hat{H}_{e-\text{ph}, s}^{(\alpha), \beta} = & i \sqrt{\frac{\hbar}{2L_1 L_2 \tilde{\rho}_s^{(\alpha)}(\vec{q}) \omega_s^{(\alpha)}(\vec{q})}} \Phi_s^{(\alpha), \beta}(x_3, q) \\ & \times (\hat{b}_s^{(\alpha)}(\vec{q}) + \hat{b}_s^{\dagger}(\vec{q})) e^{i\vec{q}\vec{r}} \end{aligned} \quad (21)$$

where $\beta = (\text{d}, \text{p}, \text{rip})$, $\hat{b}_s^{(\alpha)}(\vec{q})$ is the annihilation operator, $\hat{b}_s^{\dagger}(\vec{q})$ is the generation operator of a phonon in (α, s, \vec{q}) mode and $\Phi_s^{(\alpha), \beta}$ are the potential functions for deformation, piezoelectric, and ripple scattering interactions. Functions $\tilde{\rho}_s^{(\alpha)}(\vec{q})$ are computed according to the orthonormal conditions of Eq. (20). The potential function for the deformation interaction is defined as

$$\Phi_s^{(\alpha), d}(x_3, q) = a_{2c} \vec{q} \vec{w}_s^{(\alpha)}(x_3, q) - a_{1c} \frac{dw_{3,s}^{(\alpha)}(x_3, q)}{dx_3} \quad (22)$$

where a_{1c} and a_{2c} are the deformation constants for the conduction band. Numerical values of these constants were selected in line with those reported in Ref. [29]. One can see from Eq. (22) that the symmetry of function $\Phi_s^{(\alpha), d}$ coincides with the symmetry of the polarization vector component $w_{1,s}^{(\alpha)}$. Thus the even deformation potential corresponds to normal SA mode and vice versa.

The piezoelectric potential function induced by (α, s, q) acoustic phonon mode is found from the solution of the Poisson equation given by

$$\begin{aligned} \varepsilon(x_3) \left(\frac{d^2 \Phi_s^{(\alpha), p}(x_3, q)}{dx_3^2} - q^2 \Phi_s^{(\alpha), p}(x_3, q) \right) \\ + \frac{d\varepsilon(x_3)}{dx_3} \frac{d\Phi_s^{(\alpha), p}(x_3, q)}{dx_3} = \frac{e}{\varepsilon_0} \frac{d}{dx_3} \left(e_{33}(x_3) \frac{dw_{3,s}^{(\alpha)}(x_3, q)}{dx_3} \right) \\ - \frac{e}{2\varepsilon_0} e_{15}(x_3) q^2 w_{3,s}^{(\alpha)}(x_3, q) - \frac{e}{\varepsilon_0} q \left(\frac{e_{15}(x_3)}{2} - e_{31}(x_3) \right) \\ \times \frac{dw_{1,s}^{(\alpha)}(x_3, q)}{dx_3} - \frac{e}{\varepsilon_0} q \frac{de_{31}(x_3)}{dx_3} w_{1,s}^{(\alpha)}(x_3, q) \end{aligned} \quad (23)$$

where ε_0 is the permittivity of free space, $e_{i,k}$ ($i = 1, 2, 3$; $k = 1, \dots, 6$) are the piezoelectric modules for the hexagonal crystal. Numerical values of $e_{31}(x_3)$, $e_{33}(x_3)$ are

taken from Ref. [29], $e_{51}(x_3)$ are from Ref. [36] and the static dielectric constant $\varepsilon(x_3)$ is from Ref. [30]. Since the out-of-structure piezoelectric polarization $P_{\text{out}}^p = 0$, the Maxwell boundary conditions for the piezoelectric potential function $\Phi_s^{(\alpha),p}(x_3, q)$ at the outside surface of the structure acquire the form

$$\begin{aligned} -\varepsilon_0 \varepsilon(x_3) \left[\frac{d\Phi_s^{(\alpha),p}(x_3, q)}{dx_3} \right]_{\text{out}} \\ = -\varepsilon_0 \varepsilon(x_3) \left[\frac{d\Phi_s^{(\alpha),p}(x_3, q)}{dx_3} \right]_{\text{in}} [-eP_{3,s}^{(\alpha),p}]_{\text{in}} \\ x = -\frac{d}{2} \pm 0 \quad ("+" \text{ in}; "-" \text{ out}) \quad \text{or} \\ x = +\frac{d}{2} \pm 0 \quad ("+" \text{ out}; "-" \text{ in}) \end{aligned} \quad (24)$$

where

$$P_{3,s}^{(\alpha),p}(x_3, q) = e_{31}(x_3)qw_{1,s}^{(\alpha)}(x_3, q) - e_{33}(x_3)\frac{dw_{3,s}^{(\alpha)}(x_3, q)}{dx_3}$$

It follows from Eq. (23) that the symmetry of function $\Phi_s^{(\alpha),p}$ is the same as the symmetry of the polarization vector component $w_{3,s}^{(\alpha)}$. As a result, the even piezoelectric potential corresponds to normal AS mode and vice versa.

We write the potential function for the ripple interaction as in Ref. [39]:

$$\begin{aligned} \hat{\Phi}_s^{(\alpha),\text{rip}}(x_3, q) = \frac{dV_b(x_3)}{dx_3} w_{3,s}^{(\alpha)}(x_3, q) \\ - \frac{\hbar^2}{2} \nabla \left(\frac{d}{dx_3} \left(\frac{1}{m_{\perp}(x_3)} \right) w_{3,s}^{(\alpha)}(x_3, q) \nabla \right) \end{aligned} \quad (25)$$

It follows from Eq. (24) that the symmetry of the function $\Phi_s^{(\alpha),\text{rip}}$ is opposite to the symmetry of the polarization vector component $w_{3,s}^{(\alpha)}$. Thus, the even ripple potential corresponds to the normal SA mode and vice versa.

Functions $\Phi_{s=0}^{(\text{AS}),p}$ for a GaN slab ($d = 2$ nm) and for the type A heterostructure ($d = 10$ nm) are shown in Figure 15(a). Note that the functions for the GaN slab and AlN/GaN/AlN heterostructure with equal thicknesses are similar. For small phonon wave vectors q the absolute value of the function in the heterostructure with $d = 10$ nm and in the slab of the same thickness is more than the absolute value of this function in the structure with $d = 2$ nm. This leads to the enhancement of piezoelectric interaction with increasing structure thickness for the electrons with relatively small momentum, e.g., for non-degenerate electron gas at low temperatures.

3.3. Confined Electron–Confined Phonon Scattering Rates

The quantum mechanical probability of the system transition from the initial state i to the final state f due to electron–phonon interaction can be calculated according to

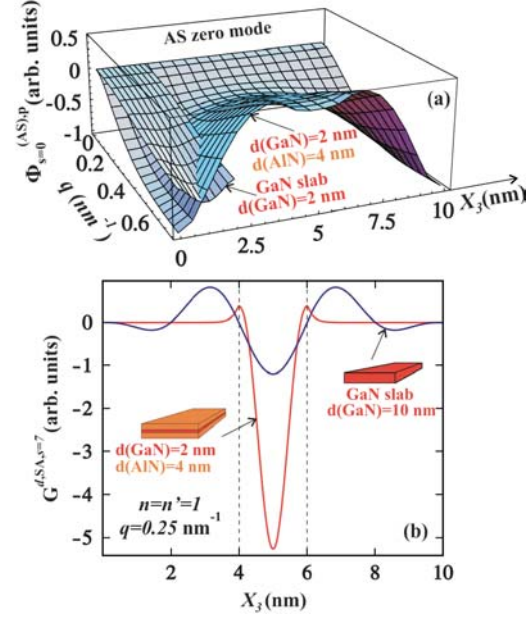


Fig. 15. (a) Piezoelectric potential for the AS zero normal mode ($s = 0$) as a function of the phonon wave vector q and coordinate x_3 shown for the slab ($0 < x_3 < 2$ nm) and for the type A heterostructure ($0 < x_3 < 10$ nm). (b) Integrand function $G_{d,SA,s=7}^{d,SA,s=7}(x_3)$ of the scattering rate matrix element for the deformation potential interaction in the GaN slab (10 nm) and type A heterostructure. Boundaries of the GaN heterostructure core layer are indicated by two vertical dashed lines. Reprinted with permission from [20], E. P. Pokatilov et al., *J. Appl. Phys.* 95, 5626 (2004). © 2004, American Institute of Physics.

Fermi's golden rule

$$\tau^{-1}(\varepsilon_i) = \frac{2\pi}{\hbar} \sum_f | \langle f | H_{e-ph} | i \rangle |^2 \delta(\varepsilon_f - \varepsilon_i) \quad (26)$$

where summation is performed over all finite states of a system. Eq. (26) determines the number of electron–phonon collisions per second, e.g., scattering rate, with which the electron transfers from some initial state i with energy ε_i to the finite state f with energy ε_f . Calculation of the relaxation time using Eq. (26) allows one to compare the intensities of electron–phonon interaction for different interaction mechanisms or, for the same mechanism, compare the scattering rates in different structures.

For the remainder of the chapter we will assume that the upper sign in the momentum conservation law $\vec{k}' = \vec{k} \pm \vec{q}$ corresponds to phonon absorption while the lower sign corresponds to phonon emission. Taking into account this conservation law and, after integration over an angle in the cylindrical coordinate system, one can rewrite Eq. (26) in the following form

$$\begin{aligned} \tau_{n,n'}^{-1}(\varepsilon) = \frac{1}{2\pi\hbar^2k} \sum_{\alpha,\beta,s} m_{\perp,n'} \int_0^\infty \frac{(N_s^{(\alpha)} + \frac{1}{2} \mp \frac{1}{2}) dq}{\tilde{\rho}_s^{(\alpha)}(q) \omega_s^{(\alpha)}(q) \sqrt{1 - (\Delta^\mp)^2}} \\ \times \left(\int_{-\frac{d}{2}}^{\frac{d}{2}} G_{n,n'}^{\beta,\alpha,s}(q, x_3) dx_3 \right)^2 \end{aligned} \quad (27)$$

where N_s^α is the phonon equilibrium occupation number, $\omega_s^{(\alpha)}$ is the phonon frequency, and functions Δ^\mp and $G_{n,n'}^{\beta,\alpha,s}$ are given as

$$(\Delta^\pm) = \frac{m_{\perp,n'}}{kq\hbar^2} \left\{ \varepsilon_{n'}^0 - \varepsilon_n^0 + \frac{\hbar^2 k^2}{2} \left(\frac{1}{m_{\perp,n'}} - \frac{1}{m_{\perp,n}} \right) + \frac{\hbar^2 q^2}{2m_{\perp,n'}} \mp \hbar \omega_s^{(\alpha)}(q) \right\} \quad (28)$$

$$G_{n,n'}^{\beta,\alpha,s}(q, x_3) = \Phi_s^{(\alpha),\beta}(q, x_3) \psi_{n'}^*(x_3) \psi_n(x_3) \quad (29)$$

Note that in Eq. (27), $n = n'$ corresponds to intrasubband transitions, and $n \neq n'$ corresponds to intersubband transitions. The electron size quantization energy in heterostructures with a thickness on the order of several nanometers, is much larger than the electron thermal energy at room temperature. In this case, one can assume that only one subband ($n = 1$) is occupied, and intersubband transitions are possible for the non-equilibrium system state, which can be created, for example, by optical excitation.^{40,41}

The function $G_{n=1,n'=1}^{SA,s=7,d}(x_3, q = 0.25 \text{ nm}^{-1})$, is depicted in Figure 15(b) for the GaN slab ($d = 10 \text{ nm}$) and for the type A heterostructure. In the slabs, the electron interacts mainly with the lowest modes ($s = 0, 1, 2$, Ref. [27] while in the heterostructures the electron interacts intensively with all modes ($s = 0, 1, 2, 3 \dots$). In Figure 15(b) one can see the strength of the interaction between an electron in the ground state and seventh normal acoustic SA mode.

3.4. Comparison of the Scattering Rates and Discussion

Calculated intrasubband scattering rates $\tau^{-1}(\varepsilon)$ in GaN slab and heterostructures are presented in Figures 16 and 18. In Figures 16(a–b) one can see the scattering rates in the GaN slab with the thickness $d = 2 \text{ nm}$. The confined electron–confined phonon scattering rates in type A and type B heterostructures are shown in Figures 17(a–b) and 18(a–b), respectively. One can notice in these figures that the phonon absorption processes $\tau_{\text{abs}}^{-1}(\varepsilon)$ are described by the smooth functions due to the fact that all phonon modes participate in the absorption process, although with different contributions determined by the value of the matrix element. The functional dependence is different for the phonon emission processes $\tau_{\text{em}}^{-1}(\varepsilon)$ where the well-defined steps are clearly seen at energies $\varepsilon_{\text{step}} = \hbar \omega_s^{(\alpha)}(q = 0)$. This corresponds to the beginning of phonon emission when the phonon energy equals to the electron energy. These characteristic steps distinguish the confined electron–confined phonon scattering rates in heterostructures from the scattering rates for free electrons interacting with bulk phonons for which the relaxation rate is proportional to the square root of electron energy ε , i.e., $\tau^{-1} \sim (\varepsilon)^{1/2}$. The calculated scattering rates are also different from the confined electron–bulk acoustic phonon scattering rates shown in

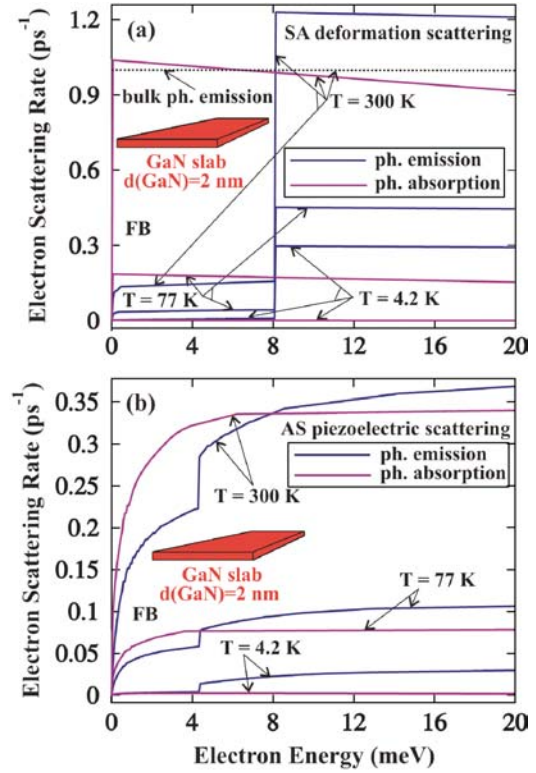


Fig. 16. Intrasubband electron scattering rate for SA normal modes as a function of the electron energy in GaN slab ($d = 2 \text{ nm}$) at three different temperatures of 4.2 K, 77 K, and 300 K. Solid lines correspond to phonon emission and dashed lines correspond to phonon absorption. The results are presented for the deformation potential interaction (a), and for the piezoelectric field interaction (b). For comparison, the bulk phonon emission is shown with the dotted curve. Reprinted with permission from [20], E. P. Pokatilov et al., *J. Appl. Phys.* 95, 5626 (2004). © 2004, American Institute of Physics.

Figure 16(a) with the dotted line (phonon emission at $T = 300 \text{ K}$; $\tau_{\text{abs}}^{-1} = \tau_{\text{em}}^{-1}$). More discussion on the difference between electron–confined phonon and electron–bulk phonon scattering rates in crystals of cubic structure can be found in Refs. [6, 7, 27, 39]. One can also notice in Figure 16 that since in the “thin” GaN slab with $d = 2 \text{ nm}$ the phonon quantization is stronger than in type A and in type B heterostructures with $d = 10 \text{ nm}$ (see Figs. 17 and 19), the first steps in the “thin” slab are shifted to higher energies.

The number of normal branches in the heterostructure can be estimated as d/c_{1c} , where c_{1c} is the lattice constant ($c_{1c} = 0.51 \text{ nm}$ for GaN [29]). Our calculations have shown that inclusion of the higher phonon branches does not influence the results (within the calculation error of $\sim 0.5\%$). It follows from this estimate that two normal modes (bulk like $s = 0$ and quantized $s = 1$) of each polarizations (SA and AS) are in the “thin” GaN slab, whereas ten normal modes of SA and AS polarizations are in both type A and type B heterostructures (including two modes

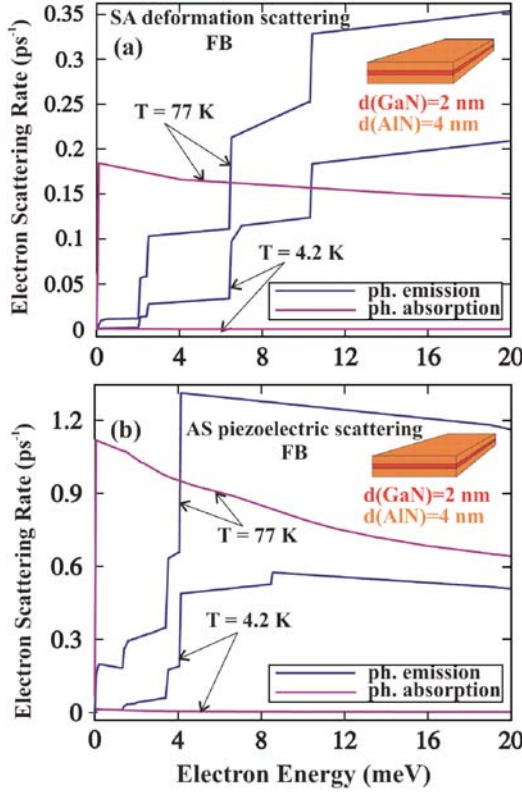


Fig. 17. Intracubband electron scattering rate for SA normal modes as a function of the electron energy in the type A heterostructure at two different temperatures of 4.2 K and 77 K. Solid lines correspond to phonon emission and dashed lines correspond to phonon absorption. The results are presented for the deformation potential interaction (a), and for the piezoelectric field interaction (b). Reprinted with permission from [20], E. P. Pokatilov et al., *J. Appl. Phys.* 95, 5626 (2004). © 2004, American Institute of Physics.

with $s = 0$, which are bulk like). The distinctive feature of scattering rates $\tau^{-1}(\varepsilon)$ in heterostructures is the involvement of the higher phonon modes into the emission processes. Figure 15(b) shows that higher phonon modes in heterostructures intensively interact with electrons due to confinement of the electron in the heterostructure core layer. In the type B heterostructure the electron wave function is shifted to the heterostructure surface by the built-in electric field. Therefore the symmetry with respect to the central plane is broken. As a result, the electron deformation potential interaction with AS modes and the electron piezoelectric interaction with SA modes emerge, while the deformation potential interaction with SA modes and the piezoelectric interaction with AS modes become weaker. Note that in the type A heterostructure, the built-in electric field does not practically influence the value of $\tau^{-1}(\varepsilon)$ because of the small potential bias.

The dependence of the scattering rate on the nanostructure thickness (See Figs. 16(a) and 17(a)) is a manifestation of the size quantization effect in electron–phonon interaction. There is no such effect in bulk because of

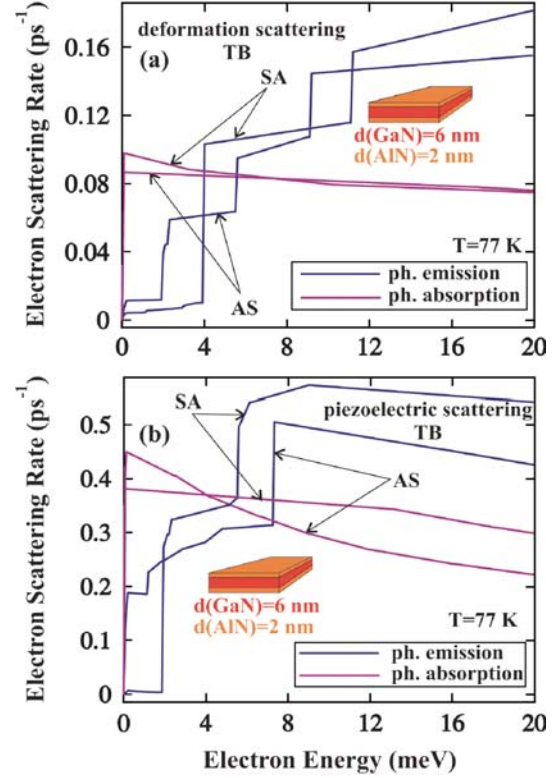


Fig. 18. Intracubband electron scattering rate for SA and AS normal modes as a function of the electron energy in the type B heterostructure at the temperature of 77 K. Solid lines correspond to phonon emission and dashed lines correspond to phonon absorption. The results presented for the deformation potential interaction (a), and for the piezoelectric field interaction (b). Reprinted with permission from [20], E. P. Pokatilov et al., *J. Appl. Phys.* 95, 5626 (2004). © 2004, American Institute of Physics.

the increase in the number of normal acoustic modes, which is proportional to V (where V is the sample volume) and is compensated by the decrease in their amplitudes $\sim V^{-1/2}$ while computing the scattering rate τ^{-1} . Analogously, in nanostructures the number of normal acoustic modes increases as $\sim d$ and the amplitude of each modes decreases as $\sim d^{-1/2}$. At the same time, the efficiency of the deformation potential interaction of electrons with the higher normal acoustic phonon modes in a thicker heterostructure is weakened (see Fig. 17). As a result, the scattering rate decreases with increasing thickness d (compare Figs. 16(a) and 17(a)).

The piezoelectric potential interaction is a long-distance interaction. To estimate its dependence on the structure thickness, we can write, using Eq. (23), the following expression $|\Phi^{p,d}| \sim d|w_s^{(a)}| \sim d^{1/2}$. This general dependence can be strongly modified by the change of the sign of the function $\Phi_s^p(x_3, q)$ for large values of s and q . Comparing Figure 16(b) with Figure 17(b) one can see that the increase of the structure thickness leads to the enhancement of the piezoelectric interaction.

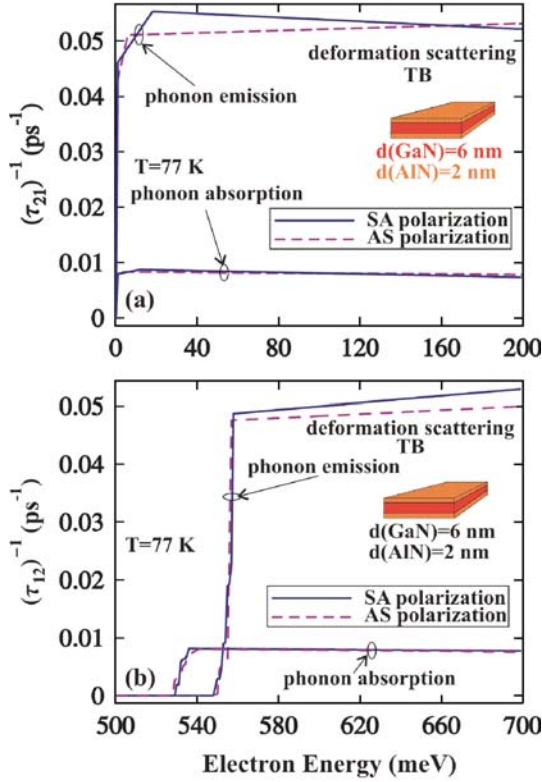


Fig. 19. Intersubband electron scattering rate for SA and AS normal modes as a function of the electron energy in the type B heterostructure at the temperature of 77 K. Solid lines correspond to SA modes while dashed lines correspond to AS modes. Panel (a) shows transitions from the excited to the ground state: $2 \rightarrow 1$; while panel (b) shows transitions from the ground to the excited state: $1 \rightarrow 2$. Reprinted with permission from [20], E. P. Pokatilov et al., *J. Appl. Phys.* 95, 5626 (2004). © 2004, American Institute of Physics.

Optical excitation of electrons into the first excited subband followed by relaxation to the ground state subband can be characterized by the function $\tau_{21}^{-1}(\varepsilon)$. This function is shown in Figure 19(a). The reverse process, due to thermal excitation, is described by the function $\tau_{12}^{-1}(\varepsilon)$ (see Fig. 19(b)). The main contribution to these transitions comes from the deformation potential interaction owing to the large value of the electron momentum. The total relaxation rates, e.g., absorption and emission processes together, $\tau^{-1}(\text{abs} + \text{em})$ are shown in Figure 20(a). The average total relaxation rates $\tau_{\text{tot}}^{-1}(T) = \sum_{\alpha, \beta} (\tau^{-1}(T))^{(\alpha), \beta}$ obtained by averaging of $(\tau^{-1}(\varepsilon))^{(\alpha), \beta}$ using the Maxwell distribution for non-degenerate electrons are presented in Figure 20(b). The resulting inequalities $\tau_{\text{tot}}^{-1}(T, \text{type A}) > \tau_{\text{tot}}^{-1}(T, \text{type B}) > \tau_{\text{tot}}^{-1}(T, 10 \text{ nm, slab}) > \tau_{\text{tot}}^{-1}(T, 2 \text{ nm, slab})$ are explained by the reasons stated above. In brief they can be formulated as follows (i) inclusion of the higher normal modes in the scattering processes in heterostructures, (ii) enhancement of the piezoelectric potential interaction ($\sim d^{1/2}$) and weakening of the deformation potential interaction ($\sim d^{-1/2}$) with the increasing

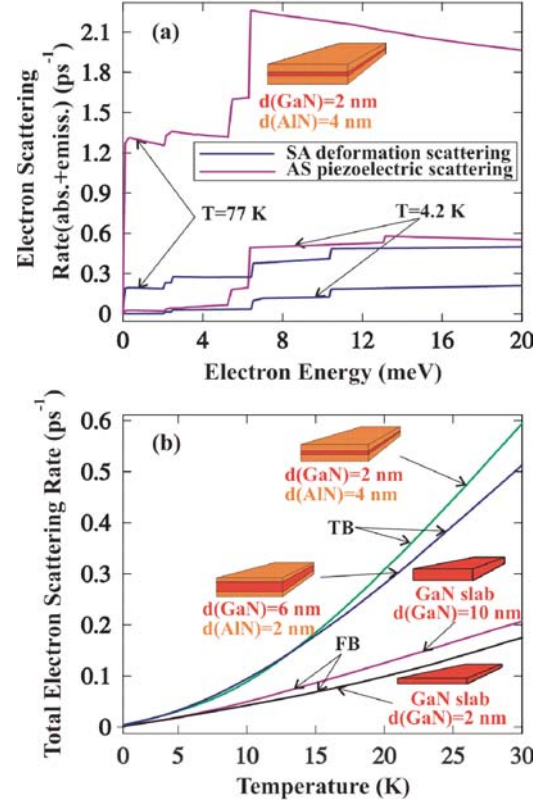


Fig. 20. (a) Combined (absorption + emission) electron scattering rate as a function of the electron energy in the type A heterostructure at two different temperatures of 4.2 K and 77 K. Solid lines correspond to the deformation potential interaction of SA normal modes and dashed lines correspond to the piezoelectric field interaction of AS normal modes. (b) Total confined electron-confined phonon scattering rate obtained by integration over all polarizations for both deformation potential and piezoelectric field interactions as a function of temperature. The results are shown for two different slab thicknesses ($d = 2 \text{ nm}$ and $d = 10 \text{ nm}$) and two different heterostructures: type A (4 nm/2 nm/4 nm) and type B (2 nm/6 nm/2 nm). Reprinted with permission from [20], E. P. Pokatilov et al., *J. Appl. Phys.* 95, 5626 (2004). © 2004, American Institute of Physics.

layer thickness d . In the structures without piezoelectric polarization the inequalities are different from the previous case and are given as $\tau_{\text{tot}}^{-1}(T, 2 \text{ nm, slab}) > \tau_{\text{tot}}^{-1}(T, \text{type A}) > \tau_{\text{tot}}^{-1}(T, \text{type B}) > \tau_{\text{tot}}^{-1}(T, 10 \text{ nm, slab})$. Therefore, the fast claddings decrease the electron-phonon interaction in the materials without the built-in electric field and, correspondingly, increase the electron mobility in such heterostructures in comparison with the generic slab without the claddings.

Figures 21(a–c) presents the intra-subband scattering rates $\tau_{11}^{-1}(T)$ for type A heterostructure as well as for the “thick” ($d = 10 \text{ nm}$) and “thin” ($d = 2 \text{ nm}$) GaN slabs. Figures 21(a) and (b) correspond to the deformation and piezoelectric potential scattering, respectively. Figure 21(c) shows the total scattering rate defined as

$$\tau_{11, \text{tot}}^{-1}(T) = \sum_{\beta} \tau_{11, \beta}^{-1}(T) \quad (30)$$

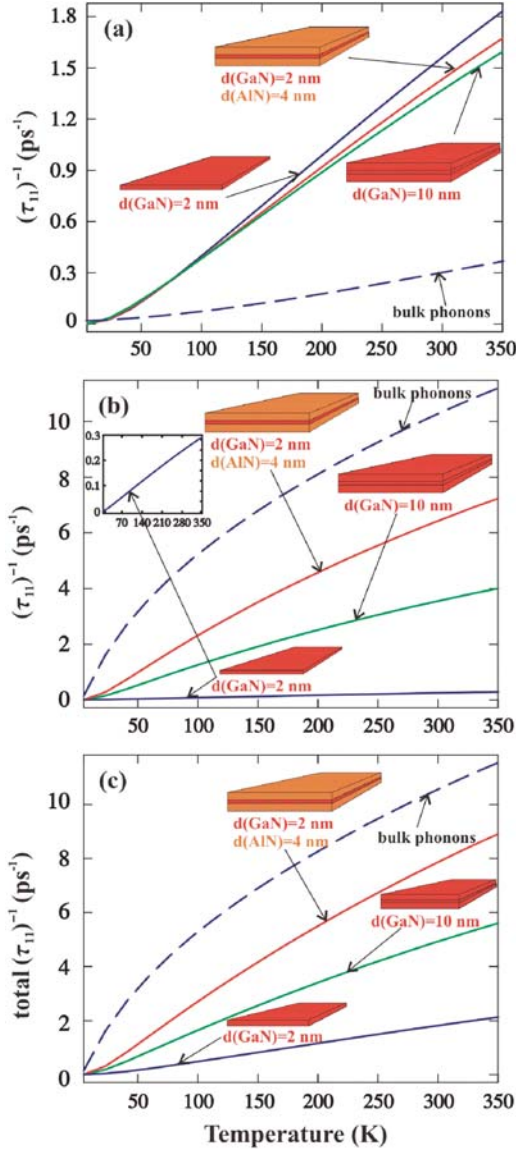


Fig. 21. Intra-subband confined electron-confined acoustic phonon scattering rates $\tau_{11,\beta}^{-1}(T)$ ($\beta = \text{def}, \text{p}$) for the acoustically mismatched heterostructures on the basis of GaN. The scattering rates in the core layer of the heterostructure or slab are shown for the (a) deformation potential scattering, and (b) piezoelectric potential scattering. The total scattering rate $\tau_{11,\text{tot}}^{-1}(T) = \sum_{\beta} \tau_{11,\beta}^{-1}(T)$, $\beta = \text{def}, \text{p}, \text{rip}$ is shown in the panel (c).

where $\beta = \text{d}, \text{p}, \text{rip}$. The contribution of the ripple interaction for a given type of heterostructure is small ($<1\%$) so that $\tau_{11}^{-1}(T)$ curves are not shown, but the contribution of this relaxation mechanism is accounted for in the sum. Figure 21(a) shows the scattering rates for the deformation potential confined electron-confined phonon interaction with SA acoustic phonon modes only. The interaction of the confined electrons in the first subband with AS phonon modes is prohibited due to the symmetry of the electron wave function. For simplicity, when calculating

the electron wave functions in 2 nm GaN well layer, it is assumed that the spontaneous and piezoelectric field effect do not lead to a significant tilting of the carrier band structure.

The scattering rates obtained using the confined electron wave function and bulk phonons are also presented in Figure 21 by the dashed lines. As one can see from this figure, there scattering rates are different from the scattering rates obtained using the confinement phonon modes for both deformational and piezoelectric scatterings. Therefore, while calculating the electron scattering rates in nanostructures one has to take into account both the electron and phonon confinement. It follows from Figure 21 that the scattering rate due to the deformation potential in type A heterostructure is smaller than that in the thin slab, while the total scattering rate in the heterostructure is larger than in the thin slab due to the strong piezoelectric scattering in the heterostructure.

Concluding this section, we established that in thin three-layered wurtzite heterostructures the electrons have stronger coupling to the high-energy phonon modes than in the slabs. This effect may be useful in design of high-frequency GaN-based devices when a fast electron relaxation is required. It has also been observed that in thicker heterostructures the built-in electric field enhances electron interaction with AS phonon modes via deformation potential and with SA phonon modes via piezoelectric potential. At the same time, the total scattering rate $\tau_{\text{SA}}^{-1} + \tau_{\text{AS}}^{-1}$ remains approximately constant with the variation of the built-in electric field. In the considered heterostructures piezoelectric interaction plays the main role in the intrasubband scattering while the deformation potential interaction dominates the intersubband scattering. The results obtained for confined electron-confined phonon interaction in wurtzite AlN/GaN/AlN thin heterostructures extend the concept of phonon engineering and can be used for optimization of GaN-based electronic and spintronic devices.

4. PHONON DISTRIBUTION IN THE ACOUSTICALLY MISMATCHED HETEROSTRUCTURES

In this section we show that modification of the acoustic phonon spectrum in heterostructures with the large acoustic impedance mismatch $\eta_{\text{core}}/\eta_{\text{cladding}}$ at the interface between the core and cladding layers results in the strong nonuniform distribution of the phonon modes in heterostructure layers (in Ref. [19] this effect was called the *phonon depletion* in the acoustically hard layer). The latter is achieved if the heterostructure parameters (thickness and mass density) are properly tuned and the cladding layers are acoustically slower and softer than the core layer, i.e., $V_{\text{s}}^{\text{Core}} > V_{\text{s}}^{\text{Cladding}}$ and $\eta^{\text{Core}} > \eta^{\text{Cladding}}$. The discussion in this section mostly follows Ref. [19] with some minor terminology changes. To describe the effect, one can solve the elasticity equation using the standard approach (see

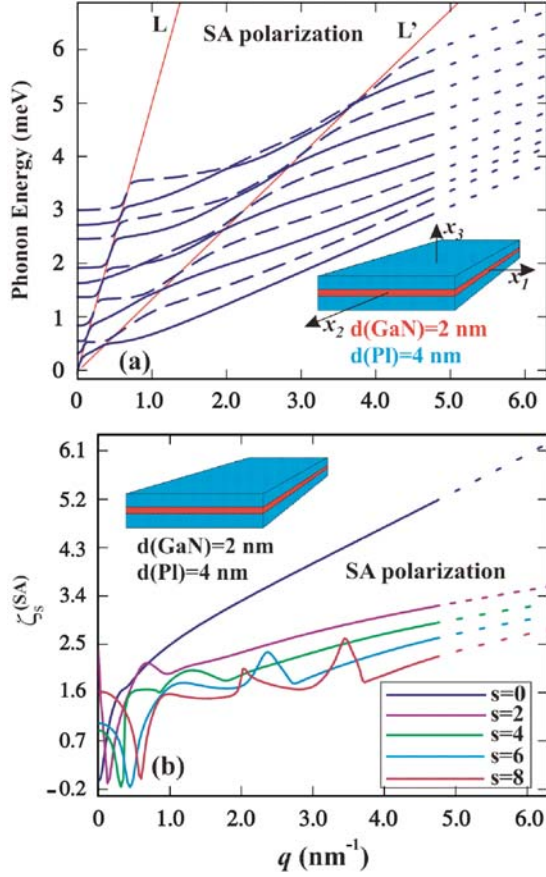


Fig. 22. (a) Phonon dispersion $\hbar\omega_s^\alpha(q)$ for symmetric (SA) hybrid acoustic phonon modes in the acoustically mismatched heterostructure. Solid and dashed curves correspond to even and odd phonon modes, respectively. (b) Phonon depletion coefficient for even SA phonon modes in the core layer of the acoustically mismatched heterostructures. Reprinted with permission from [19], E. P. Pokatilov et al., *Appl. Phys. Lett.* 85, 825 (2004). © 2004, American Institute of Physics.

Section 2) and choose the free-surface boundary (FSB) conditions at the outside boundaries of the heterostructure. Such approach combined with FSB was shown to give accurate results for slab and wire geometries.^{7, 14, 27} We verified that the use of clamped-surface boundaries at the outside surface of the heterostructure leads to quantitatively similar results.

4.1. Phonon Distribution in the Embedded Acoustically Hard Thin Films

Figure 22(a) shows phonon dispersion branches $\hbar\omega_s^\alpha(x_3, q)$ for SA polarization in plastic/GaN/plastic heterostructure with dimensions 4 nm/2 nm/4 nm. As one can see, the dispersion for zero mode ($s = 0$) is similar to the transverse acoustic (TA) phonon mode in bulk plastic with sound velocity $v \approx 1$ km/s. Other dispersion branches ($s = 1, 2, \dots$) correspond to quantized quasi-optical. In Figure 22(a) the lowest phonon branches $s = 1, 2, \dots, 9$

are shown. The continuum approach does not limit the number of quantized phonon branches. We assume that the number of all branches, which participate in the electron-phonon interaction, is not larger than the ratio d/c (for wurzite GaN $c = 0.51$ nm). The quasi-optical branches have parabolic type dispersion ($\omega \sim q^2$) for phonon wave vectors close to the Brillouin zone center with characteristic sharp change of the slope indicated by the straight line L. The slope along L is close to the sound velocity of the bulk TO phonon in GaN (~ 4 km/s). This narrow region of q values with drastic change in the dispersion slope is dominated by the elastic properties of the acoustically fast core layer. For all other values of q , the slopes of the dispersion curves are significantly smaller. It means that the average group velocity of the phonon modes for a given dispersion curve, which extend through the whole heterostructure, is between the bulk TA and longitudinal acoustic (LA) phonon velocities in the acoustically soft and slow plastic (the region near the LA bulk mode velocity of 1.6–1.9 km/s is denoted by line L'). The width of the regions with the high velocity is relatively small (~ 0.1 nm⁻¹). Thus, in average vibrational properties of the considered heterostructure are dominated by the acoustically slow cladding materials.

To elucidate the phonon depletion effect, we introduce a new parameter, phonon depletion coefficient, through the energy considerations. The total lattice vibration energy in heterostructure is given by⁴²

$$E = \frac{1}{2} \int_V \rho(x_3) \dot{\vec{U}}^2 dV + \frac{1}{2} \int_V c_{iklm}(x_3) U_{ik} U_{lm} dV \quad (31)$$

where $U_{ik} = (1/2)((\partial U_i/\partial x_k) + (\partial U_k/\partial x_i))$, and modules of elasticity of heterostructure layers $c_{iklm} = c_{iklm}(x_3)$. Here, the first term represents kinetic energy and the second term is potential energy of the lattice oscillations. Substituting Eqs. (18)–(19) to Eq. (31), and using orthonormalization condition of Eq. (20), we can write the energy of the normal mode in the form

$$E_s^{(\alpha)}(q) = E_{s,1}^{(\alpha)}(q) + E_{s,2}^{(\alpha)}(q) \\ = (\omega_s^{(\alpha)})^2 |A_s^{(\alpha)}|^2 \left(\rho_1 \int_1 |\vec{w}_s^{(\alpha)}|^2 dx_3 + \rho_2 \int_2 |\vec{w}_s^{(\alpha)}|^2 dx_3 \right) \quad (32)$$

where indices 1 and 2 are related to the core and cladding layers of the heterostructure, respectively. The terms in Eq. (32) are structured in such a way that the first one corresponds to the energy $E_{s,1}(q)$ of elastic vibrations of the (α, s, q) normal mode in the core layer while the second one to the energy of vibrations $E_{s,2}(q)$ in the cladding (barrier) layers. We now define the phonon depletion coefficient $\xi_s^{(\alpha)}(q)$ as a ratio of the elastic energy inside the core layer to the elastic energy in the whole heterostructure (both energies are taken per unit volume)

$$\xi_s^{(\alpha)}(q) = \frac{E_{s,1}^{(\alpha)}(q)}{V_1} \frac{V}{E_s^{(\alpha)}(q)} = \frac{d}{d_1} \frac{\rho_1}{\rho_s^{(\alpha)}} \int_1 |w_s^{(\alpha)}(q, x_3)|^2 dx_3 \quad (33)$$

where $V_1 = L_1 L_2 d_1$ and $V = L_1 L_2 d$. According to this definition, $\xi_s^{(\alpha)}(q)$ shows the relative amount of lattice vibrational energy inside the core layer with respect to the total energy per unit thickness of the heterostructure. It is also illustrative to compare the mean square polarization vectors of the normal modes in the core layer of the heterostructure with the mean square polarization vectors in slabs (thin films without cladding layers that affect the phonon dispersion). For this purpose, we introduce the phonon damping coefficient $r_s(q, d)$ defined as

$$r_s^{(\alpha)}(q, d) = \frac{d_1 \int_{-d/2}^{d/2} |\vec{w}_{s,sl}^{(\alpha)}(q, x_3)|^2 dx_3}{d \int_{-d_1/2}^{d_1/2} |\vec{w}_{s,h}^{(\alpha)}(q, x_3)|^2 dx_3} \quad (34)$$

where $\vec{w}_{s,sl}^{(\alpha)}(q, x_3)$ is the polarization vector $\vec{w}_s^{(\alpha)}(q, x_3)$ in the slab with thickness d and $\vec{w}_{s,h}^{(\alpha)}(q, x_3)$ is the polarization vector $\vec{w}_s^{(\alpha)}(q, x_3)$ in the heterostructure.

In Figure 22(b) we presented the logarithm of the phonon-depletion coefficient taken with negative sign, i.e., $\zeta_s^{(SA)}(q) = -\log_{10} \xi_s^{(SA)}(q)$, as a function of q . The results are shown for even SA polarization modes of the plastic/GaN/plastic heterostructure with dimensions 4 nm/2 nm/4 nm. For almost all values of q the $\zeta_s^{(SA)}(q)$ values are positive. Moreover, for $q \geq 2 \text{ nm}^{-1}$, the $\zeta_s^{(SA)}$ value is approximately 2, which means that phonon energy density in acoustically slow cladding layers of the heterostructure exceeds the phonon energy density in the acoustically fast core layer by the two orders of magnitude. Thus, in such acoustically mismatched heterostructures, where $V_s^{\text{Core}} > V_s^{\text{Cladding}}$ and $\eta_s^{\text{Core}} > \eta_s^{\text{Cladding}}$ and the layer thickness is sufficiently small ($d_i \ll \Lambda$) a significant depletion of phonons in the core layer is observed. It is important to note here that the phonon depletion takes place for all modes and over almost all values of q . Only phonons within the narrow wave-vector interval that corresponds to the maximum-slop region of the dispersion curves (line L in Fig. 22(a)) make up an exception. The minima of the $\zeta_s^{(SA)}$ curves in Figure 22(b) correspond to the regions of sharp slope change in Figure 22(a). In such regions (where $\zeta_s^{(SA)} \leq 0$ (see Fig. 22(b))) the phonons are localized in the core layer. For all other values of q the phonons in the core layer are practically absent (phonon depletion).

In Figure 23 we compare the mean square polarization vector $\vec{w}_s^{(\alpha)}(q, x_3)$ for the analogous phonon modes of the acoustically mismatched heterostructure and generic slab. Figure 23(a) shows the phonon-damping coefficient $\log_{10} r_s^{(\alpha)}(q, d = 10 \text{ nm})$. The thickness of the slab ($d = 10 \text{ nm}$) is chosen equal to the total thickness of the heterostructure. One can see from this figure that the mean square polarization vectors in GaN core layer is almost two orders of magnitude less than those in the slab. This result holds over a wide range of the phonon wave vector q values. The narrow regions of q , where $\log_{10} r_s^{(\alpha)}(q, d) \leq 0$, are also clearly seen from the graphs.

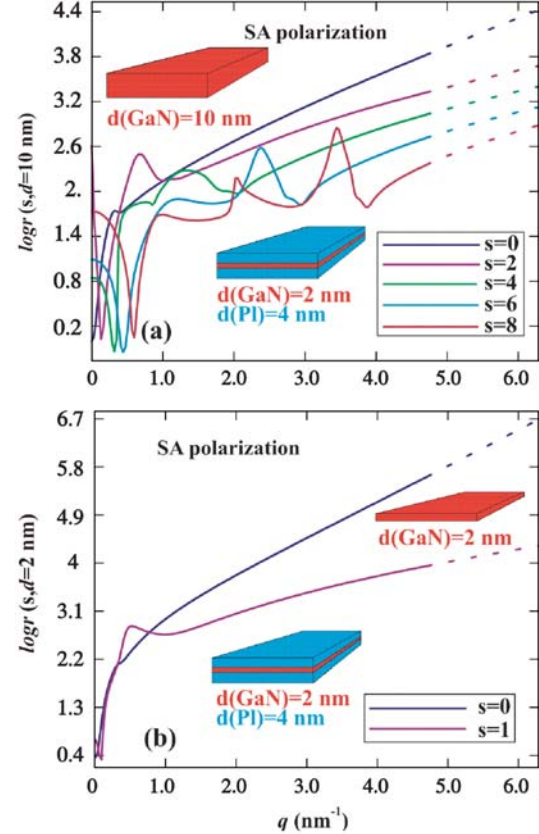


Fig. 23. Phonon damping coefficient for even SA phonon modes: (a) Comparison of the square mean displacement in the GaN slab and in the acoustically mismatched heterostructure of the same thickness; (b) the same as in (a) but the thickness of the slab is chosen the same as the thickness of the heterostructure core layer. Reprinted with permission from [19], E. P. Pokatilov et al., *Appl. Phys. Lett.* 85, 825 (2004). © 2004, American Institute of Physics.

It is even more illustrative to compare the lattice vibrations in the core layer of the heterostructure with those in the GaN slab of the same thickness as the core layer, i.e., $d = 2 \text{ nm}$. We will consider two lowest branches for GaN slab. Figure 23(b) shows the damping coefficient $\log_{10} r_s^{(\alpha)}(q, d = 2 \text{ nm})$ for both modes. The mean square polarization vectors in the slab exceed that one in the core layer of the acoustically mismatched heterostructure by many orders of magnitude for almost all q . The lattice vibrations are strongly damped in the heterostructure core in wide intervals of q .

The physical origin of the described phonon concentration in the cladding layers (or depletion in the core layer) of the acoustically mismatched heterostructure is redistribution of the displacement $\vec{U}_s^{(\alpha)} \sim A_s^{(\alpha)} \vec{w}_s^{(\alpha)}(x_3)$, which leads to the situation when there are much less lattice vibrations in the core layer than in the acoustically slow cladding layers. The latter is illustrated in Figure 24, which shows the components $w_{i,s=1}^{\text{SA}}(x_3, q)$ (a) and $w_{3,s=1}^{\text{SA}}(x_3, q)$ (b) of the vibration amplitude vector

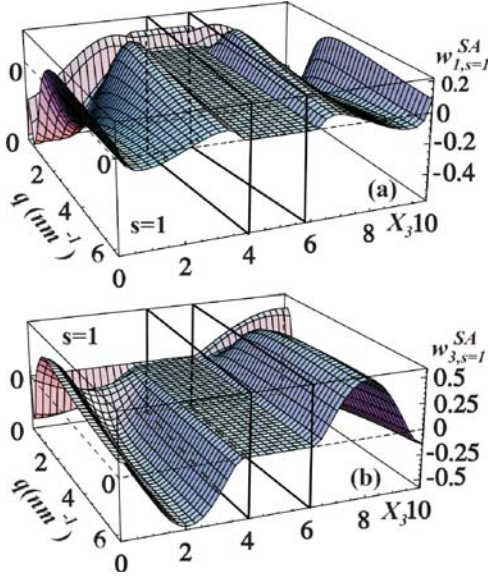


Fig. 24. Components $w_{1,s=1}^{SA}(x_3, q)$ (a) and $w_{3,s=1}^{SA}(x_3, q)$ (b) of the vibration amplitude vector $\mathbf{w}_{1,s=1}^{SA}(x_3, q)$ as the functions of the phonon wave vector q and coordinate x_3 . Reprinted with permission from [19], E. P. Pokatilov et al., *Appl. Phys. Lett.* 85, 825 (2004). © 2004, American Institute of Physics.

$\vec{w}_{s=1}^{(SA)}(x_3)$ as functions of q and X_3 . Note that the displacement component surfaces are nearly flat and $w_{1,s=1}^{SA}$ and $w_{3,s=1}^{SA}$ approximately equal to zero inside the core layer while the amplitudes of vibrations are high in the cladding layers. Similar dependence is observed for other SA and AS modes.

In conclusion, we demonstrated that the modification of the acoustic phonon spectrum in semiconductor heterostructures with the large acoustic impedance mismatch ($V_s^{\text{Core}} > V_s^{\text{Cladding}}$ and $\eta^{\text{Core}} > \eta^{\text{Cladding}}$) between the core and cladding layers results in the strong concentration of the phonon modes from the majority heterostructure branches in the cladding layers. The effect is achieved if the heterostructure thickness is in nanometer scale ($d \ll \Lambda$) to ensure phonon quantization. Since in Si the room-temperature Λ is on the order of 50 nm–300 nm and $\lambda_d \sim 1$ –2 nm, the latter requirement can be met for realistic state-of-the-art heterostructures.^{23–24}

5. ACOUSTIC PHONON PROPERTIES OF NANOWIRES WITH ELASTICALLY DISSIMILAR BARRIERS

In this section we describe the acoustic phonon spectra and phonon propagation in the rectangular and cylindrical nanowires embedded within the elastically dissimilar materials. As example systems we consider GaN nanowires with AlN and plastic barrier layers. Our discussion in this section mostly follows Refs. [15–16]. The barriers with the lower sound velocity compress the phonon

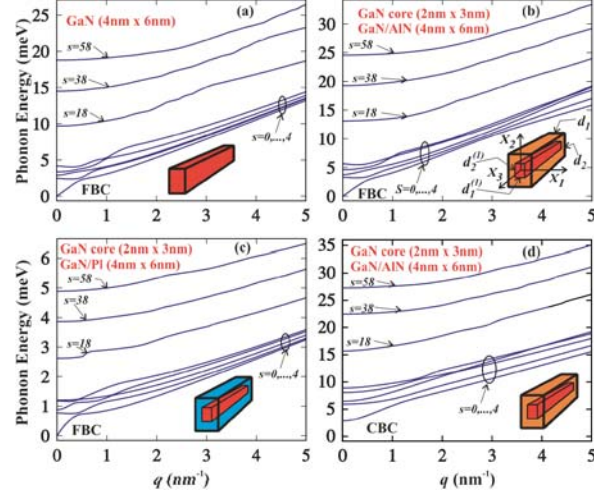


Fig. 25. Phonon dispersions for the dilatational modes for free-surface (a–c) and clamped-surface (d) boundary conditions at the external barrier boundaries. The results are shown for (a) GaN nanowire of the 4 nm × 3 nm cross section without the barriers; (b, d) GaN nanowire with acoustically fast AlN barriers of the 4 nm × 6 nm and 2 nm × 3 nm GaN nanowire cross sections; (c) GaN nanowire with acoustically slow barriers of the 4 nm × 6 nm and 2 nm × 3 nm GaN nanowire cross sections.

energy spectrum and reduce the phonon group velocities in the nanowire. The barriers with the higher sound velocity have an opposite effect. The physical origin of this effect is related to re-distribution of the elastic deformations in the acoustically mismatched nanowires.

5.1. Theoretical Model for the Rectangular Nanowires with Barriers

We consider a generic rectangular nanowire, which forms a potential quantum well, confined in a rectangular barrier shell (see insets to Fig. 25). As an example material system we have chosen a nanowire made of GaN. At the same time, our calculation procedure can be applied to any combination of the nanowire and barrier materials. It is assumed that GaN crystal lattice has wurtzite structure with reference axis c along the nanowire axis. The axis X_3 of the Cartesian coordinate system is directed along the c axis, while axis X_1 and axis X_2 are in the cross-sectional plane of the nanowire, parallel to its sides (see insets to Fig. 25). The origin of the coordinate system is in the center of the nanowire. The lateral dimensions of the rectangular nanowire itself are denoted by $d_1^{(1)}$ and $d_2^{(1)}$ while the total lateral dimensions (nanowire thickness plus barrier thickness) are d_1 and d_2 , correspondingly. The lateral dimensions of the nanowire are chosen in nanometer range in order to ensure size quantization of the acoustic phonon spectrum. Since the considered nanostructure is homogeneous along the direction of X_3 , and inhomogeneous in the (X_1, X_2) plane, we look for the solution of the Eq. (1) in the following form

$$U_i(x_1, x_2, x_3, t) = u_i(x_1, x_2) e^{i(\omega t - k x_3)}, \quad (i = 1, 2, 3) \quad (35)$$

Substituting Eq. (35) in Eq. (1), we can write three equations for the components of the displacement vector

$$\begin{aligned} (c_{44}q^2 - \omega^2\rho)u_1 &= c_{11}\frac{\partial^2 u_1}{\partial x_1^2} + c_{66}\frac{\partial^2 u_1}{\partial x_2^2} + \frac{\partial c_{11}}{\partial x_1}\frac{\partial u_1}{\partial x_1} + \frac{\partial c_{66}}{\partial x_2}\frac{\partial u_1}{\partial x_2} \\ &+ (c_{12} + c_{66})\frac{\partial^2 u_2}{\partial x_1 \partial x_2} + \frac{\partial c_{12}}{\partial x_1}\frac{\partial u_2}{\partial x_2} + \frac{\partial c_{66}}{\partial x_2}\frac{\partial u_2}{\partial x_1} \\ &+ q(c_{13} + c_{44})\frac{\partial u_3}{\partial x_1} + q\frac{\partial c_{13}}{\partial x_1}u_3 \end{aligned} \quad (36)$$

$$\begin{aligned} (c_{44}q^2 - \omega^2\rho)u_2 &= c_{66}\frac{\partial^2 u_2}{\partial x_1^2} + c_{11}\frac{\partial^2 u_2}{\partial x_2^2} + \frac{\partial c_{66}}{\partial x_1}\frac{\partial u_2}{\partial x_1} + \frac{\partial c_{11}}{\partial x_2}\frac{\partial u_2}{\partial x_2} \\ &+ (c_{12} + c_{66})\frac{\partial^2 u_1}{\partial x_1 \partial x_2} + \frac{\partial c_{66}}{\partial x_1}\frac{\partial u_1}{\partial x_2} + \frac{\partial c_{12}}{\partial x_2}\frac{\partial u_1}{\partial x_1} \\ &+ q(c_{13} + c_{44})\frac{\partial u_3}{\partial x_2} + q\frac{\partial c_{13}}{\partial x_2}u_3 \end{aligned} \quad (37)$$

$$\begin{aligned} (q^2 c_{33} - \omega^2\rho) &= c_{44}\left(\frac{\partial^2 u_3}{\partial x_1^2} + \frac{\partial^2 u_3}{\partial x_2^2}\right) + \frac{\partial c_{44}}{\partial x_1}\frac{\partial u_3}{\partial x_1} + \frac{\partial c_{44}}{\partial x_2}\frac{\partial u_3}{\partial x_2} \\ &- q(c_{13} + c_{44})\left(\frac{\partial u_1}{\partial x_1} + \frac{\partial u_2}{\partial x_2}\right) - q\left(\frac{\partial c_{44}}{\partial x_1}u_1 + \frac{\partial c_{44}}{\partial x_2}u_2\right) \end{aligned} \quad (38)$$

In deriving these equations, we first made substitution $u_3 = -iu'_3$ and then renamed the variable again as $u'_3 \equiv u_3$.

The considered structure has two distinctively different symmetry planes. From the invariance of the system of Eqs. (36)–(38) for reflection operations in these planes, there are four possible types of solution.⁷ These solutions can be denoted as Dilatational modes (D): $u_1^{AS}(x_1, x_2)$; $u_2^{SA}(x_1, x_2)$; $u_3^{SS}(x_1, x_2) \rightarrow u_i^D$; Flexural₁ (F₁) and Flexural₂ (F₂): $u_1^{SS}(x_1, x_2)$; $u_2^{AA}(x_1, x_2)$; $u_3^{AS}(x_1, x_2) \rightarrow u_i^{F_1}$; $u_1^{AA}(x_1, x_2)$; $u_2^{SS}(x_1, x_2)$; $u_3^{SA}(x_1, x_2) \rightarrow u_i^{F_2}$ and Shear (Sh): $u_1^{SA}(x_1, x_2)$; $u_2^{AS}(x_1, x_2)$; $u_3^{AA}(x_1, x_2) \rightarrow u_i^{Sh}$. Here SA and AS (symmetric and asymmetric) indicate whether the mode is even or odd with respect of the operation of the sign conversion of the corresponding variable, i.e., $f(x_1, x_2) = f(-x_1, x_2) = f(x_1, -x_2) \rightarrow f^{SS}(x_1, x_2)$, $f(x_1, x_2) = -f(-x_1, x_2) = -f(x_1, -x_2) \rightarrow f^{AA}(x_1, x_2)$, etc.

The displacement vector in the arbitrary point of the nanowire can be presented as the superposition of all normal modes in the following form

$$\vec{U}(x_1, x_2, x_3) = \frac{1}{\sqrt{L_3}} \sum_{\alpha, n, k} A_n^{(\alpha)}(q, t) \vec{w}_n^{(\alpha)}(x_1, x_2, q) e^{-iqx_3} \quad (39)$$

where $A_n^{(\alpha)}(q, t)$ is the amplitude of the normal mode with the polarization (α), for the phonon branch enumerated by the quantum number n , and with the phonon wave number q . Vectors \vec{w} should satisfy the normalized

conditions, written as

$$\begin{aligned} \int \rho(x_1, x_2) \vec{w}_n^{(\alpha)}(x_1, x_2, q) \vec{w}_{n'}^{(\alpha')*}(x_1, x_2, q) dx_1 dx_2 \\ = \tilde{\rho}_n^{(\alpha)}(q) \delta_{nn'} \delta_{\alpha\alpha'} \end{aligned} \quad (40)$$

$$\int \vec{w}_n^{(\alpha)}(x_1, x_2, q) \vec{w}_{n'}^{(\alpha')*}(x_1, x_2, q) dx_1 dx_2 = \delta_{nn'} \delta_{\alpha\alpha'} \quad (41)$$

where integrals in Eqs. (40)–(41) are taken over the surfaces of the cross-sectional planes of the nanowire.

The outside boundaries of the nanowire, i.e., outside surfaces of the barrier shell, can be either clamped or free. In the case of the clamped boundaries, the boundary conditions on the outside surfaces of the nanowire barrier shell have the form $w_1 = w_2 = w_3 = 0$, while in the case of the free boundaries $P_1 = P_2 = P_3 = 0$, where $P_i = \sigma_{ik} n_k$ is the force component and n_k is the component of the unitary vector normal to the outer surface. Note, that coefficients in Eqs. (36)–(38) are functions of the ratios $\sqrt{c_{ik}/\rho}$, which define the sound velocities. The ratios $\sqrt{c_{33}/\rho} = V_{||}^L$, and $\sqrt{c_{11}/\rho} = V_{\perp}^L$, correspond to the longitudinal sound velocities along and perpendicular to the axis c , while $\sqrt{c_{44}/\rho} = V^T$ gives the transverse sound velocity. The latter explains while the mismatch of the sound velocities at the interface between the nanowire and the barrier layers plays as important a role as the acoustic impedance mismatch η .

5.2. Theoretical Models for the Cylindrical Nanowires with Barriers

A schematic view of the considered cylindrical nanowire is presented in the insets to Figure 26. To fully use the advantage of the cylindrical symmetry of structure, we use the cylindrical coordinate system with the radius vector \vec{r} and angle φ in the cross-sectional plane, and axis Z along the nanowire axis. The radius of the nanowire core is designated as R_1 while the total radius of the heteronanowire (nanowire with the barrier layer) is designated as R . The thickness of the barrier shell (coating layer) is $\Delta R = R - R_1$. Both radii are assumed to be in the nanometer scale range to ensure the phonon confinement. The length of the nanowire is considered to be infinite. The phonon energy spectrum of the freestanding nanowire without coating is also calculated for comparison with the spectra in coated nanowires.

In the cylindrical coordinate system, the displacement vector \vec{U} has the following components: $U_r(r, \varphi, z)$, $U_{\varphi}(r, \varphi, z)$, $U_z(r, \varphi, z)$. Since the considered structure is homogeneous in the Z direction, we search for the solution of Eq. (1) in the following form

$$\begin{aligned} U_r(r, \varphi, z) &= A(q) u_r(r) \cos m\varphi e^{i(\omega t - qz)} \\ U_{\varphi}(r, \varphi, z) &= A(q) u_{\varphi}(r) \sin m\varphi e^{i(\omega t - qz)} \\ U_z(r, \varphi, z) &= A(q) u_z(r) \cos m\varphi e^{i(\omega t - qz)} \end{aligned} \quad (42)$$

where $m = 0, \pm 1, \pm 2, \pm 3, \dots$. In Eq. (42), $A(q)$ is the amplitude of a normal phonon mode. Performing the

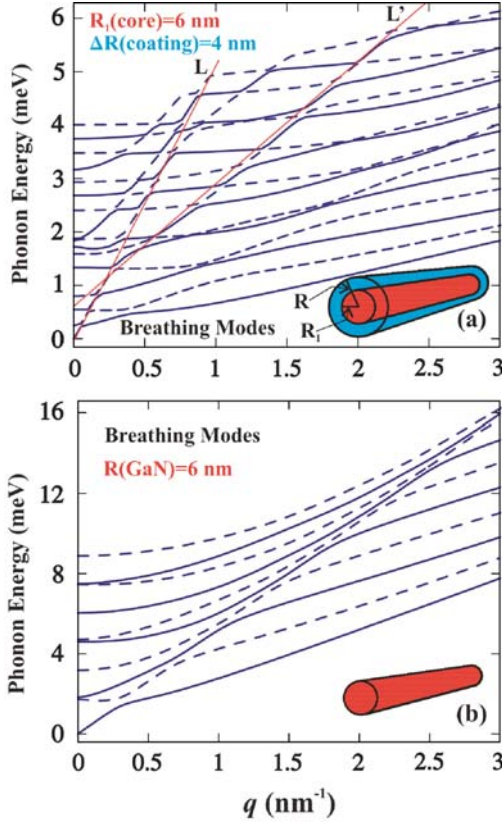


Fig. 26. Phonon energy as a function of the phonon wave vector q for the breathing modes ($m = 0$). The results are shown for (a) GaN nanowire with the “acoustically soft” barrier layer ($R_1(\text{GaN}) = 6$ nm and $R = 10$ nm); and (b) GaN nanowire without the barrier layer ($R = 6$ nm). The insets show the geometry of the nanostructures. Reprinted with permission from [16], E. P. Pokatilov et al., *Superlatt. Microstruct.* 38, 168 (2005). © 2005, Elsevier.

differentiation in Eq. (1) one needs to take into account that both the elastic modules c_{ik} and the mass density of the material ρ are the piece-wise functions of r . For numerical simulation, the piece-wise functions were replaced with the smooth functions in such a way that their shape did not influence the results.

Substituting Eq. (42) in Eq. (1), one can obtain the system of three equations for the three components of the displacement vector as

$$\begin{aligned}
 & (c_{44}q^2 - \rho\omega^2)u_r \\
 &= c_{11}\frac{d^2u_r}{dr^2} + \left(\frac{c_{11}}{r} + \frac{dc_{11}}{dr}\right)\frac{du_r}{dr} \\
 &+ \left(\frac{1}{r}\frac{dc_{12}}{dr} - \frac{c_{11}}{r^2} - \frac{m^2c_{66}}{r^2}\right)u_r \\
 &+ m\left(\frac{1}{r}\frac{dc_{12}}{dr} - \frac{c_{11} + c_{66}}{r^2}\right)u_\varphi + \frac{m(c_{11} - c_{66})}{r}\frac{du_\varphi}{dr} \\
 &+ q(c_{13} + c_{44})\frac{du_z}{dr} + q\frac{dc_{13}}{dr}u_z
 \end{aligned} \quad (43)$$

$$\begin{aligned}
 & (c_{44}q^2 - \rho\omega^2)u_\varphi \\
 &= c_{66}\frac{d^2u_\varphi}{dr^2} + \left(\frac{c_{66}}{r} + \frac{dc_{66}}{dr}\right)\frac{du_\varphi}{dr} \\
 &- \left(\frac{c_{66}}{r^2} + \frac{1}{r}\frac{dc_{66}}{dr} + \frac{c_{11}m^2}{r^2}\right)u_\varphi - \frac{m(c_{11} - c_{66})}{r}\frac{du_r}{dr} \\
 &- m\left(\frac{c_{11} + c_{66}}{r^2} + \frac{1}{r}\frac{dc_{66}}{dr}\right)u_r - \frac{mq(c_{13} + c_{44})}{r}u_z \quad (44) \\
 & (c_{33}q^2 - \rho\omega^2)u_z \\
 &= c_{44}\frac{d^2u_z}{dr^2} + \left(\frac{c_{44}}{r} + \frac{dc_{44}}{dr}\right)\frac{du_z}{dr} - \frac{c_{44}m^2}{r^2}u_z \\
 &- q\left(\frac{c_{13} + c_{44}}{r} + \frac{dc_{44}}{dr}\right)u_r - q(c_{13} + c_{44})\frac{du_r}{dr} \\
 &- \frac{qm(c_{13} + c_{44})}{r}u_\varphi
 \end{aligned} \quad (45)$$

In the case of the free-surface boundary conditions (FBC) on the outer surface of the nanowire, all components of the stress tensor are zero ($\sigma_{rr} = 0$, $\sigma_{r\varphi} = 0$, and $\sigma_{rz} = 0$) for $r = R$, which leads to the following equations

$$\begin{aligned}
 & (c_{11} - c_{12})\frac{du_r}{dr} + c_{12}\left(\frac{du_r}{dr}\frac{1}{r}u_r + \frac{m}{r}u_\varphi\right) + qc_{13}u_z = 0 \\
 & \frac{du_\varphi}{dr} - \frac{m}{r}u_r - \frac{u_\varphi}{r} = 0 \\
 & \frac{du_z}{dr} - qu_r = 0
 \end{aligned} \quad (46)$$

In the case of the clamped-surface boundary conditions (CBC) on the outer surface of the nanowire, all components of the displacement vector are zero ($u_r = 0$, $u_\varphi = 0$, $u_z = 0$) for $r = R$.

The system of Eq. (43) has a solution for any integer value of m . At $m = 0$, the system of three equations splits into subsystems of two equations for components u_r and u_z of the vector $\vec{u} = (u_r, u_z)$, and a separate equation for the $u_\varphi(r)$ function. The solutions of the system of two equations constitute the longitudinal-type “breathing” modes, which correspond to periodic dilatations and compressions of the cross-section of the nanowire. At $q = 0$, the oscillations along the radius and the axis become independent and have different frequencies. The solution of Eqs. (43)–(45) for u_φ describes the torsional oscillations around the nanowire axis. In these oscillations, the magnitude of the displacement vector is proportional to the radius and achieves its maximum on the nanowire surface. For $m \neq 0$, one needs to solve the system of the equations for all three components of the displacement vector. The solutions at $|m| = 1$ are called the bending vibrations, while the solutions at $|m| > 1$ are called the circular vibrations of m order.

5.3. Acoustic Phonon Engineering in Nanowires with Acoustically Dissimilar Barriers

The solutions of Eqs. (36)–(38) for the rectangular nanowires and Eqs. (43)–(45) for the cylindrical nanowires have been found numerically using the finite difference method. In this section we present the phonon dispersion relations for all types of the phonon polarizations with both free and clamped external boundary conditions for the barrier layers. The material parameters for GaN and AlN required for our calculations have been taken from Refs. [14, 29]. Figure 25 shows the plots of the phonon dispersion for the dilatational polarization in the “bare” rectangular GaN nanowire of $4 \text{ nm} \times 6 \text{ nm}$ cross-section (Fig. 25(a)), GaN nanowire with AlN barriers of $4 \text{ nm} \times 6 \text{ nm}$ and $2 \text{ nm} \times 3 \text{ nm}$ nanowire cross-section (Figs. 25(b, d)) and GaN nanowire with plastic barriers of $4 \text{ nm} \times 6 \text{ nm}$ and $2 \text{ nm} \times 3 \text{ nm}$ nanowire cross-section (Fig. 25(c)).

The phonon dispersions in Figure 25(d) are plotted for the clamped boundary conditions (CBC) at the outside surface of the barrier layers. The rest of the curves are plotted for the free-surface boundary conditions (FBC) at the outside surface of the barrier layers. In the case of the clamped outside boundaries the bulk-like phonon branches are absent in the phonon spectra, and all phonon energy levels are size quantized. As one can see from the comparison of the plots in Figures 25(b) and (d), the change of the outside boundary conditions from the free surface to the clamped surface leads to enhancement of the size quantization in the low-energy part of the phonon spectrum but only weakly influence the high-energy branches. The latter can be explained by the fact that the position of the high-energy levels is mostly determined by the inverse of the lattice parameter $1/a$, whereas the size quantization in the low-energy part of the spectrum depends on $1/d$.

The influence of the elastic properties of the barrier shells are seen very well in the dilatational phonon spectra of the embedded nanowires. The acoustically soft and slow plastic barrier layers lead to the increased density of the phonon branches per energy interval while the acoustically fast AlN barrier layers lead to the density decrease. In the nanowire of $4 \text{ nm} \times 6 \text{ nm}$ cross-section the energy interval of 6 meV (see Fig. 25(a)) includes the first 9 branches for $q = 0$. In the nanowires with the acoustically soft plastic barriers the same number of low-energy levels fits into a considerably less energy interval of only 1.8 meV. In the case of GaN nanowire with the acoustically fast AlN barrier layers the first 9 levels are positioned entirely within the 7.5 meV energy interval in Figure 25(b) for FBC and in the 11 meV energy interval in Figure 25(d) for CBC. In comparison with generic slabs, i.e., thin films, the phonon spectrum of nanowires with and without barrier layers is characterized by lower density of phonon branches per unit energy interval.

In Figure 26(a) we present the breathing modes for cylindrical GaN nanowire with the core radius $R_1 = 6 \text{ nm}$

embedded into the acoustically soft plastic shell with the thickness $\Delta R = 4 \text{ nm}$. The total radius of the coated nanowire is $R = 10 \text{ nm}$. Each of the dispersion curves in the coated nanowire has narrow regions with distinctively different slopes. The steep segments of the dispersion curves reflect the properties of the “acoustically fast” material (GaN in this case). These segments can be approximated by a straight line, which is indicated in Figure 26(a) by the symbol L. The slope of the straight line L is close to the sound velocity of the bulk transverse acoustic (TA) phonons in GaN. The slope of the straight line L' is close to the sound velocity of the bulk longitudinal acoustic (LA) phonons in the plastic material. It is interesting to note that the extent of the regions with the small slopes (in momentum space) is approximately one order of magnitude larger than the extent of the regions with the steep slopes although the cross-section area of “acoustically slow” material is only a factor of two larger than the cross-section area of the “acoustically fast” material. Another effect produced by the acoustically mismatched barrier layer is the compression of the confined phonon branches (increased number of branches per energy interval). The latter can be seen from the comparison of the spectrum in Figure 26(a) with that of the nanowire without coating shown in Figure 26(b). The breathing modes in uncoated GaN nanowire are calculated for the radius $R = 6 \text{ nm}$, which is equal to the radius of the coated nanowire core in Figure 26(a). In Figure 26(a), there are 16 dispersion branches confined in the energy interval of 3.1 meV, while in Figure 26(b) there are 10 branches in the wider energy interval of 9 meV.

Similar features can be seen in the spectra of the torsional oscillations with $m = 0$. Figure 27(a) shows the torsional phonon modes in the nanowire with the core radius $R_1 = 6 \text{ nm}$ and the barrier shell thickness $\Delta R = 2 \text{ nm}$. For comparison, Figure 27(b) presents the torsional phonon modes for the uncoated GaN nanowire with the radius $R = 6 \text{ nm}$. The dispersion of the torsional phonon modes in cylindrical nanowires resembles that of the shear phonon modes in thin films.¹⁴ The torsional vibrations in the coated nanowire (which are also transverse) are hybridized. Their structure reflects the different acoustic properties of the nanowire core and the barrier shell.

Figure 28(a) shows the circular phonon modes of the order ($m = \pm 2$) in the nanowire with the core radius $R_1 = 6 \text{ nm}$ and barrier shell thickness $\Delta R = 2 \text{ nm}$. For comparison in Figure 28(b), the same modes are presented for the nanowire without the barrier shell (coating). The amplitude of the oscillations for torsional modes periodically changes along the circumference while the directions of the vectors $u_{\perp} = (u_r, u_{\varphi})$ are anti-parallel at the opposite ends of the nanowire diameter.

The phonon group velocity dependence on the frequency for different type of modes in the coated and uncoated rectangular and cylindrical nanowires is presented in Figures 29 and 30, respectively. The phonon

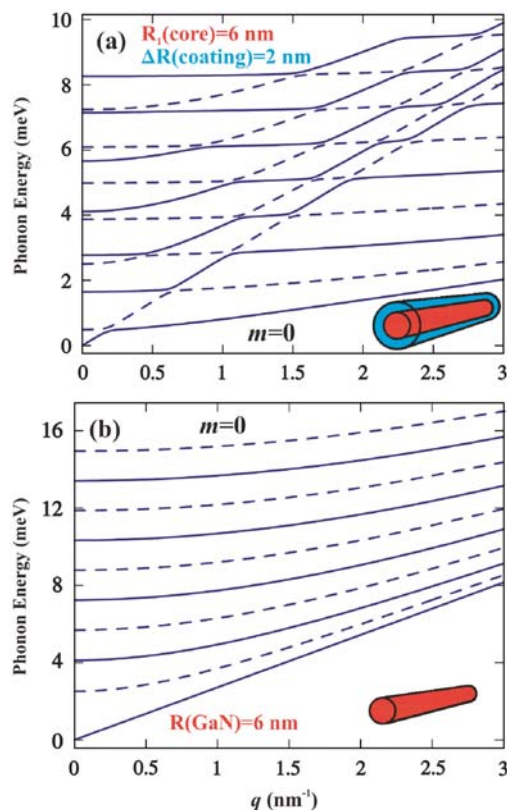


Fig. 27. The same as in Figure 26 but for the torsional phonon modes with $m = 0$. Reprinted with permission from [16], E. P. Pokatilov et al., *Superlatt. Microstruct.* 38, 168 (2005). © 2005, Elsevier.

group velocities for the coated nanowires are shown within the range of energies where the predictions of the continuum approximation are unambiguous. The group velocity curves $\bar{v}(\omega)$ are strongly oscillating functions due to the presence of many quantized phonon branches $s(\omega)$ and the fast variation of the derivatives $(v_s^{(\alpha)}(\omega))^{-1} = dq_s^{(\alpha)}(\omega)/d\omega$ with changing ω .

One can see in Figures 29–30, that the presence of the acoustically soft and slow plastic barriers has led to a strong reduction of the phonon group velocity by factor of 3 in both cylindrical and rectangular nanowires in comparison with bare GaN nanowires. The presence of AlN barriers leads to an opposite effect of increasing by factor of 1.3 the phonon group velocity in the nanowire (see Fig. 30). It is important to point out that a simple averaging of the elasticity modules and mass densities in the considered nanowires with the barrier layers, like it is done in the effective medium approximations,²⁴ would not have led to such strong velocity dependence on the barrier structure.

In summary, the acoustically mismatched nanowire coating (barrier shell) introduces significant modification to the phonon spectrum and group velocities. Moreover, different types of the phonon modes are sensitive to both the coating material and its thickness. The latter opens

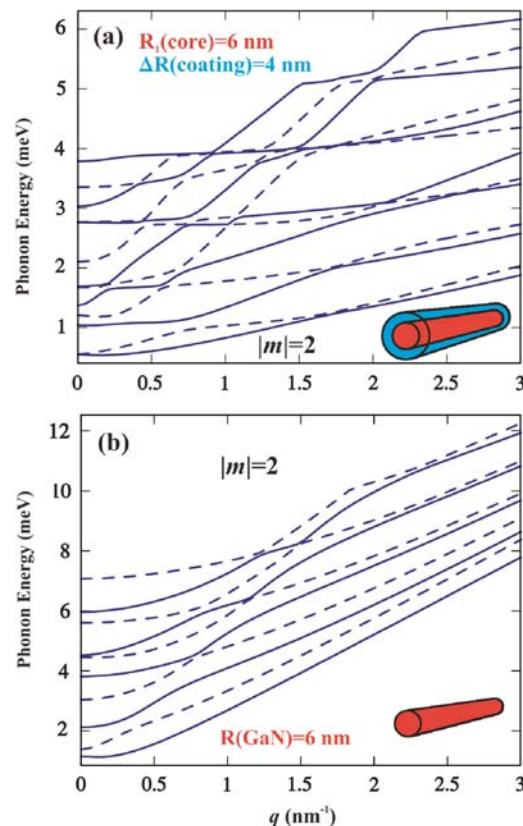


Fig. 28. The same as in Figure 26 but for the circular phonon modes of the order $m = 0$. Reprinted with permission from [16], E. P. Pokatilov et al., *Superlatt. Microstruct.* 38, 168 (2005). © 2005, Elsevier.

up a possibility of the phonon transport tuning in the acoustically mismatched nanowires by a proper selection of the barrier parameters. The acoustic impedance and sound velocity mismatch at the nanowire–barrier interface introduces important additional degrees of freedom

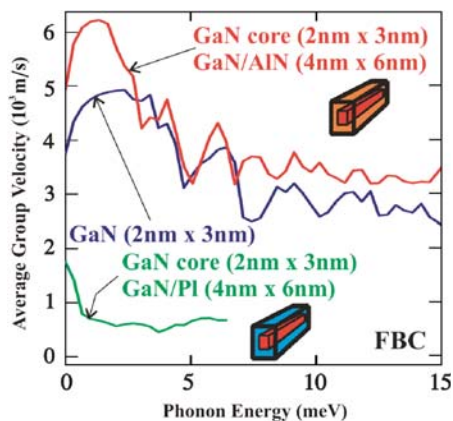


Fig. 29. Averaged phonon group velocity as a function of the phonon frequency for dilatational modes in the rectangular GaN nanowire with AlN and plastic coatings.

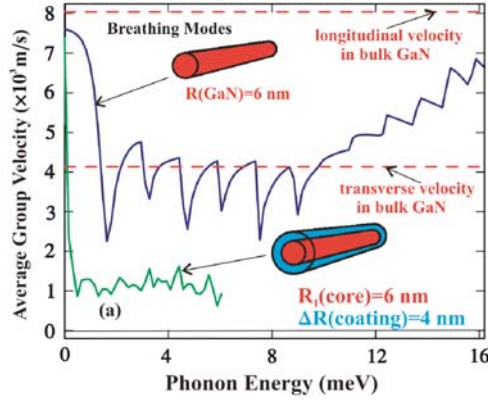


Fig. 30. Averaged phonon group velocity as a function of the phonon frequency for breathing modes in the cylindrical GaN nanowire with the “acoustically soft” barrier layer ($R_1(\text{GaN}) = 6 \text{ nm}$, $R = 10 \text{ nm}$) and the uncoated GaN nanowire ($R = 6 \text{ nm}$). Reprinted with permission from [16], E. P. Pokatilov et al., *Superlatt. Microstruct.* 38, 168 (2005). © 2005, Elsevier.

and can become important tuning parameters for phonon engineering.^{23,24}

6. ENHANCEMENT OF THE ELECTRON MOBILITY LIMITED BY OPTICAL PHONONS

The electron mobility in polar semiconductors at room temperature and above is limited by the electron–phonon scattering.⁴⁴ The intensity of the electron–phonon interaction in semiconductor heterostructures depends on the electron wave function and energy spectrum as well as on the optical and acoustic phonon dispersion. Changing geometry and material parameters of heterostructures one can affect both the carrier and phonon spectrum. In this section we show that heterostructures made of wurtzite AlGaIn/GaN/AlGaIn offer an extra degree of freedom in tuning the electron–phonon interaction via adjustment of their built-in electric field or introduction of shallow $\text{In}_x\text{Ga}_{1-x}\text{N}$ channel-nanogroove in the middle of the GaN potential well. Our discussion in this section mostly follow Refs. [21–22].

6.1. Electron–Optical Phonon Interactions and Electron Mobility in Wurtzite Heterostructures

Electron–optical phonon interactions define many important properties of semiconductors and manifest themselves in polaronic effects, appearance of the broad impurity absorption bands, etc.⁴⁴ In the kinetic processes the optical phonons play an important role by limiting the electron mobility at high temperatures. The reported calculations of the electron mobility in nanostructures are usually limited to two special cases: (i) thick and (ii) ultra-thin conductive channels. In the first case the bulk approach is used and the

electron confinement, phonon confinement, and interaction between electron and interface phonons are not taken into account. In the second case it is assumed that only the ground electron subband is occupied and the inter-subband electron transitions can be neglected.^{45,46} However, in heterostructures with nanometer scale conduction channels ($d > 5 \text{ nm}$), which are important for practical applications, the energy distance between the quantized electron levels $\Delta\epsilon_{n,n-1} = \epsilon_n^0 - \epsilon_{n-1}^0$ (ϵ_n^0 is the energy of n -th quantized level) can be smaller than the optical phonon energy and the inter-subband electron transitions play an important role.^{21–22}

In order to account for the inter-subband transitions in QWs we derived in Ref. [21] the system of two integral equations for the electron kinetic relaxation times. This system is the extension of the Boltzmann transport equation introduced in the convenient form in Ref. [27]. The system of two integral equations has been modified to include the phonon dispersion. The modified equations, derived under the assumption of a spherical electron Brillouin zone, are written as

$$\sum_{\vec{p}', m=\pm 1, \lambda, n'=1,2} \left[W(n, \vec{p} \rightarrow n', \vec{p}') \frac{(1 - f^0(\epsilon_n + m \cdot \hbar \omega_\lambda(q)))}{(1 - f^0(\epsilon_n))} \times \left(\tau_n(\vec{p}) - \tau_{n'}(\vec{p}') \frac{\vec{p} \cdot \vec{p}'}{p^2} \right) \right] = 1 \quad (47)$$

where $n = 1, 2$. In Eq. (1) $W(\gamma \rightarrow \gamma') = (2\pi/\hbar) |\langle \gamma | \hat{H}_{\text{IF}}^S + \hat{H}_{\text{IF}}^A + \hat{H}_C^S + \hat{H}_C^A | \gamma' \rangle|^2 \delta(E_\gamma - E_{\gamma'})$ is the probability of a transition of the electron–phonon system from the state γ with energy E_γ to the state γ' with the energy $E_{\gamma'}$, $f^0(\epsilon) = (\exp((\epsilon - \epsilon_F)/(k_B T)) + 1)^{-1}$, ϵ is the electron energy, \vec{p} and \vec{p}' are the electron momentum in the initial and final states, λ is the quantum number of the confined and interface optical phonon branches, $\tau_1(\epsilon)$ is the kinetic relaxation time of an electron with energy ϵ in the first (ground) subband, which includes electron transitions within the first subband ($1 \leftrightarrow 1$) and transitions from the first to the second subband ($1 \rightarrow 2$), $\tau_2(\epsilon)$ is the kinetic relaxation time of an electron in the second subband, which includes transitions from the second to the first subband ($2 \rightarrow 1$) and the transitions within the second subband ($2 \leftrightarrow 2$).

The Hamiltonians of interaction of electrons with the symmetric (S) and asymmetric (A), confined (C) and interface (IF) optical phonon modes, i.e., \hat{H}_{IF}^S , \hat{H}_{IF}^A , \hat{H}_C^S , and \hat{H}_C^A , in wurtzite heterostructures were taken from Ref. [47]. We have calculated the drift electron mobility $\mu_{(T)}$ using the equation obtained by extending the standard formalism¹ to include the inter-subband transitions

$$\mu(T) = \frac{e}{k_B T} \frac{\sum_{n=1}^2 (1/m_{\perp,n}) \int_0^\infty \epsilon \tau_n(\epsilon) f^0(\epsilon) (1 - f^0(\epsilon)) d\epsilon}{\sum_{n=1}^2 \int_0^\infty f^0(\epsilon_n^0 + \epsilon) d\epsilon} \quad (48)$$

where $m_{\perp,n}$ is the effective electron mass, averaged by electron wave functions of n -th energy level (see Eq. (17))

from Section 3). To solve Eq. (47) we generated a mesh with the step of 0.2 meV. The upper boundary energy of $\varepsilon_{\max} = 600$ meV was chosen from the condition $\varepsilon_{\max} \gg \hbar\omega_{\text{opt}}$. The system of $2N$ ($N = 3001$) linear equations for the values of τ_1 and τ_2 in the nodal points ε_l ($l = 1, \dots, N$) has been solved numerically. The system of the equations was terminated with the condition $\varepsilon_l + \hbar\omega(q) \approx \varepsilon_N$ when $\varepsilon_l + \hbar\omega(q) > \varepsilon_N$ ($\varepsilon_N = \varepsilon_{\max} \gg \hbar\omega_{\text{opt}}$). The calculated relaxation times were plugged into Eq. (48) to obtain the mobility.

6.2. Electric Field Effect on the Electron Mobility in Wurtzite AlN/GaN/AlN Heterostructures

The strong built-in electric field, characteristic for AlN/GaN interface, creates a triangular potential well in GaN layer. In Figure 31 we show the electron wave function (w.f.) for the ground ($n = 1$) and the first excited ($n = 2$) states in AlN(3 nm)/GaN(6 nm)/AlN(3 nm) heterostructure, which are confined along z -axis (growth direction). Z -axis coincides with c crystallographic direction and originates in the middle of QW. The electric field value indicated in Figure 31 is the difference between the built-in and external field, i.e., $\mathcal{F} = F_{\text{built-in}} - F_{\text{ext}}$. The value of \mathcal{F} determines the slope of the potential well in the GaN layer. When $\mathcal{F} = 0$, the built-in electric field is entirely compensated by the perpendicular external field: $F_{\text{built-in}} = F_{\text{ext}}$. To better elucidate the effect it is assumed that the carrier concentration is not affected by the external field. Since the barrier height is ~ 1.918 eV the electrons do not spill over and can move only along the QW layer. As the QW slope increases, the electron w.f. for the ground $\Psi_{n=1}(z) = \Psi_{n=1}^s(z)$ and excited $\Psi_{n=2}(z) = \Psi_{n=2}^a(z)$ states are squeezed to the heterostructure interface.

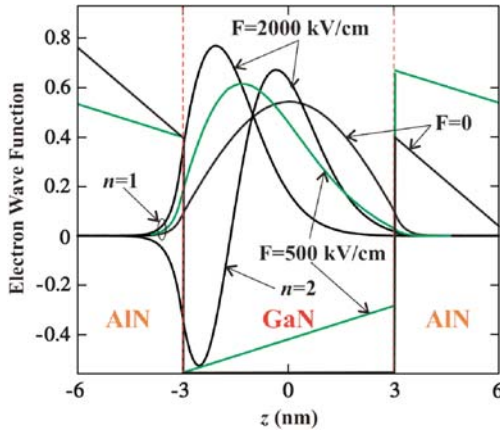


Fig. 31. Electron wave functions for the ground and first excited subbands in AlN/GaN/AlN heterostructure with different value of the perpendicular electric field F , which is defined as the difference between the built-in (spontaneous and induced polarization) and the compensating external field, i.e., $\mathcal{F} = F_{\text{built-in}} - F_{\text{ext}}$. Reprinted with permission from [21], E. P. Pokatilov et al., *Appl. Phys. Lett.* 89, 113508-1 (2006). © 2006, American Institute of Physics.

The energy of the ground and the first excited electron states in the flat QW ($\mathcal{F} = 0$) with the width $d_1 = 6$ nm is equal to $\varepsilon_1^0 = 40.8$ meV and $\varepsilon_2^0 = 163.3$ meV, respectively. In QW with the uncompensated field $\mathcal{F} = 2000$ kV/cm, it is $\varepsilon_1^0 = 388$ meV and $\varepsilon_2^0 = 731.6$ meV, respectively. The confined optical phonon energies in such heterostructure are in the intervals 69.2 meV–69.3 meV and 90.8 meV–91.9 meV, while the interface optical phonon energies are in the intervals 69.5 meV–72.9 meV and 91.8 meV–110.4 meV. We determined the optical phonon spectra in such heterostructure using equations from Ref. [48]. Our calculations show that for relevant carrier concentrations ($N_s = 10^{12} \text{ cm}^{-2}$ – $N_s = 10^{13} \text{ cm}^{-2}$) the mobility in QW with the compensated field ($\mathcal{F} = 0$) is limited by the inter-subband transitions ($1 \leftrightarrow 2$) rather than the intra-subband transitions ($1 \leftrightarrow 1$). The latter is true even in the case when the phonon energy $\hbar\omega_{\max}$ only slightly exceeds the energy $\varepsilon_2^0 - \bar{\varepsilon}$ required for the inter-subband transition. For the non-degenerate electron gas (NEG) the energy $\bar{\varepsilon}$ is defined as $\bar{\varepsilon} = \varepsilon_1^0 + k_B T$ while for the degenerate electron gas (DEG) $\bar{\varepsilon}$ is equal to the Fermi energy ε_F . Since the third subband is much higher in energy ($\varepsilon_3^0 = 367.4$ meV for $\mathcal{F} = 0$) its effect is negligible. Thus when the optical phonon energy is comparable with the energy difference $\varepsilon_2^0 - \bar{\varepsilon}$ the inter-subband transitions dominate the scattering.

In the framework of our theoretical approach one can make the following observations. The intra-subband scattering in the ground state ($1 \leftrightarrow 1$) is determined by the matrix element $M_{11} = \int_{-d/2}^{d/2} \Psi_{n=1}^2 V_{\text{IF,C}}^{S,A} dz$, where d is the width of the whole heterostructure, $V_{\text{IF,C}}^{S,A}$ is the potential for the S (symmetric), A (asymmetric), C (confined), and IF (interface) optical phonon modes. With increasing electrical field this matrix element increases mostly due to the w.f. $\Psi_{n=1}(z)$ shift to the QW interface and growth of its maximum (see Fig. 31). For $\mathcal{F} = 0$, only S phonon modes contribute to the matrix element. The intensity of the inter-subband electron transitions ($1 \leftrightarrow 2$) is determined by (i) the value of the energy difference $\varepsilon_2^0 - \bar{\varepsilon}$ and (ii) the matrix element $M_{12} = \int_{-d/2}^{d/2} \Psi_{n=1} \Psi_{n=2} V_{\text{IF,C}}^{S,A} dz$. When $\varepsilon_2^0 - \bar{\varepsilon}$ becomes considerably larger than the phonon energy $\hbar\omega$ the inter-subband transitions stop. For $\mathcal{F} = 0$, wave function $\Psi_{n=2}$ is antisymmetric and, correspondingly, transitions are generated by antisymmetric phonon modes. A perpendicular electric field squeezes $\Psi_{n=2}$: for $F = 2000$ kV/cm both extremes are in one half of the GaN layer ($-3 \text{ nm} < z < 0$), which reduces the matrix element M_{12} . The latter, together with the increased gap between subbands, reduce the electron transitions with increasing field.

The results for room temperature mobility with the low, medium, and high electron densities are shown in Figure 32. The first observation is that increasing electron density reduces the electron mobility due to enhancement of the inequality $\hbar\omega > \varepsilon_2^0 - \varepsilon_F$, which make the

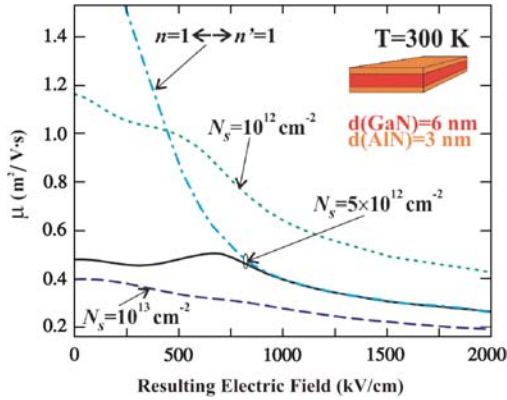


Fig. 32. Electron mobility versus perpendicular electric field in AlN/GaN/AlN heterostructure for three values of the electron concentration. Dash-dotted curve shows the mobility calculated by taking into account scattering in the ground state subband only ($N_s = 5 \cdot 10^{12} \text{ cm}^{-2}$). Reprinted with permission from [21], E. P. Pokatilov et al., *Appl. Phys. Lett.* 89, 113508-1 (2006). © 2006, American Institute of Physics.

inter-subband transitions more intensive. With increasing \mathcal{F} the energy gap between subbands widens and the intra-subband scattering becomes the only scattering mechanism. The effect of the uncompensated field $\mathcal{F} \neq 0$ is two-fold. From one side, the field reduces inter-subband scattering ($1 \rightarrow 2$), but enhances intra-subband scattering ($1 \leftrightarrow 1$). In NEG case ($N_s = 10^{12} \text{ cm}^{-2}$) in the field range $\mathcal{F} = 250\text{--}300 \text{ kV/cm}$ the transitions ($1 \rightarrow 2$) weaken and the reduction of μ slows. In the limit of high fields ($\mathcal{F} = 2000 \text{ kV/cm}$), μ is defined by the transitions ($1 \leftrightarrow 1$) with absorption of a phonon (the phonon-emission limited mobility is approximately three times larger). For $N_s = 5 \cdot 10^{12} \text{ cm}^{-2}$ the range of the fields when transitions ($1 \rightarrow 2$) dominate is wider. Weakening of the inter-subband transitions leads even to a moderate growth of μ and appearance of a maximum near $\mathcal{F} \sim 700 \text{ kV/cm}$. For fields $\mathcal{F} \sim 2000 \text{ kV/cm}$ the intra-subband transitions with the absorption and emission of a phonon became approximately equal in strength. In DEG case ($N_s = 10^{13} \text{ cm}^{-2}$) with the externally compensated built-in field ($\mathcal{F} = 0$) intra-subband transitions ($1 \leftrightarrow 1$) with phonon emission become important, while the interval of switching on the inter-subband transitions ($1 \rightarrow 2$) extends in energy. Strengthening of the electron–phonon interaction leads to nearly monotonic reduction in the carrier mobility with increasing \mathcal{F} .

Figure 33 shows the ratio of the mobility in QW with the compensated field to that with uncompensated field $\mu(\mathcal{F} = 0, T)/\mu(\mathcal{F} \neq 0, T)$ as a function of temperature T . The results are presented for three values of the uncompensated field $\mathcal{F} = 500 \text{ kV/cm}$, $\mathcal{F} = 2000 \text{ kV/cm}$ and $\mathcal{F} = 4000 \text{ kV/cm}$, electron concentrations. For NEG ($N_s = 10^{12} \text{ cm}^{-2}$) the mobility at $\mathcal{F} = 0$ is larger than that at $\mathcal{F} \neq 0$ since the electron–phonon interaction is stronger in the tilted QW with the uncompensated built-in

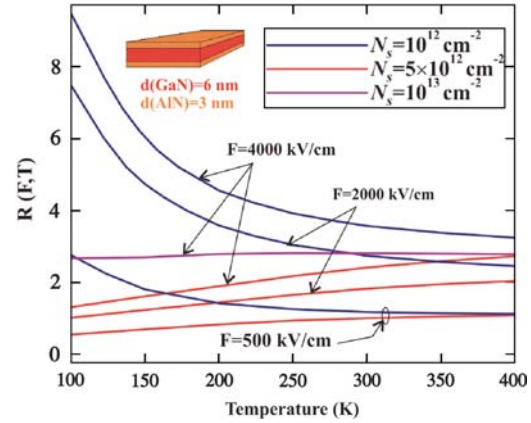


Fig. 33. Mobility enhancement coefficient $R(\mathcal{F}, T)$ as a function of temperature for three values of the electron concentration. Reprinted with permission from [21], E. P. Pokatilov et al., *Appl. Phys. Lett.* 89, 113508-1 (2006). © 2006, American Institute of Physics.

electric field. With increasing T , the mobility ratio monotonically decreases from $\sim 8 \div 9$ at $T = 100 \text{ K}$ to ~ 3 at $T = 300 \text{ K}$. One should note here that $T < 100 \text{ K}$ range requires separate consideration since at low temperatures the electron mobility is limited by acoustic phonons and impurity scattering.^{49,50} For higher $N_s = 5 \cdot 10^{12} \text{ cm}^{-2}$, the room temperature mobility is enhanced by a factor of ~ 2 for GaN QWs with the compensated electric field (with the initial built-in field between $2000\text{--}4000 \text{ kV/cm}$). In DEG case ($N_s = 10^{13} \text{ cm}^{-2}$) we observe the mobility enhancement of a factor of ~ 3 in the whole temperature range.

6.3. Electron Mobility Enhancement in AlN/GaN/AlN Heterostructures with InGaN Nanogrooves

Very recently, Indium Nitride (InN) attracted a lot of attention after it was discovered by Davydov et al.⁵¹ and confirmed by independent studies^{52–53} that its band gap is small, $E_g(\text{InN}) = 0.7 \text{ eV}$, contrary to the previously widely accepted value of nearly 2 eV . Although InN is rarely, if ever, used in devices in its binary form, when alloyed with GaN it forms a core constituent of the blue laser diode. In this letter we show that InGaN alloy utilized in electronic devices can substantially improve the room-temperature carrier mobility in wurtzite AlN/GaN/AlN heterostructures, which is limited by the polar optical phonons. Our approach for the mobility enhancement is based on the combination of the electron band-gap engineering and the phonon engineering ideas.^{10, 11, 15, 21, 54–55} In the proposed heterostructure InN is used as an example of material, which is compatible with GaN and yet has much smaller band gap.

We consider a narrow groove made of $\text{In}_x\text{Ga}_{1-x}\text{N}$ (with small In content x) inside a wurtzite AlN/GaN/AlN heterostructure, which forms a quantum well (QW). The resulting step-like profile of the confining potential is

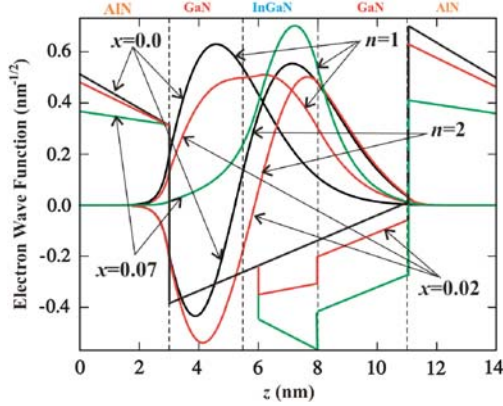


Fig. 34. Electron wave function in AlN/GaN/AlN quantum well with $\text{In}_x\text{Ga}_{1-x}\text{N}$ nanogroove for several values In content x . For $x = 0$ and $x = 0.02$ the ground ($n = 1$) and excited ($n = 2$) state wave functions are shown with the solid and dashed lines, respectively. For $x = 0.07$ only the ground state wave function is shown with the dotted line. The confining potentials for three values of In content x are indicated with the solid ($x = 0$), dashed ($x = 0.02$) and dotted ($x = 0.07$) lines. The height of the confining potential at GaN/AlN interface is 1918 meV. Reprinted with permission from [21], E. P. Pokatilov et al., *Appl. Phys. Lett.* 89, 113508-1 (2006). © 2006, American Institute of Physics.

shown in Figure 34. To demonstrate the effect we compare the electron drift mobility in the reference AlN (3 nm)/GaN (8 nm)/AlN (3 nm) QW and in QW with 2 nm-wide nanogroove, i.e., AlN (3 nm)/GaN (3 nm)/ $\text{In}_x\text{Ga}_{1-x}\text{N}$ (2 nm)/GaN (3 nm)/AlN (3 nm).

The built-in field tilts the band diagram and creates a triangular potential well, which localizes the charge carriers. We carried our calculations for two values of the built-in field $F_{\text{built-in}} = 600$ kV/cm and $F_{\text{built-in}} = 1000$ kV/cm Ref. [56]. The conduction band offset at GaN/AlN interface was estimated as $E_{\text{QW}} = 0.7 \times (E_{\text{G}}(\text{AlN}) - E_{\text{G}}(\text{GaN})) = 1918$ meV. The nanogroove does not confine the electron wave function but affects its position in the confining AlN/GaN/AlN QW. The depth of the nanogroove is calculated as $\Delta E_0 = 0.8 \times (E_{\text{G}}(\text{GaN}) - E_{\text{G}}(\text{In}_x\text{Ga}_{1-x}\text{N}))$. The band gap of $\text{In}_x\text{Ga}_{1-x}\text{N}$ is approximated as $E_{\text{G}}(\text{Ga}_{1-x}\text{In}_x\text{N}) = (1 - x)E_{\text{G}}(\text{GaN}) + xE_{\text{G}}(\text{InN}) - x(1 - x)b$, where b is the bowing parameter and $E_{\text{G}}(\text{InN}) = 0.78$ eV.²⁹ The reported values of the bowing parameter for InN vary from 1 eV to 4.5 eV, depending on the In content x .²⁹ We should note though that for all values of b from this interval we can obtain a nanogroove deep enough for our purposes. In the calculations, we used $b = 3$ eV reported in (Refs. [57, 58]) for $\text{In}_x\text{Ga}_{1-x}\text{N}$ with $x < 0.2$. The electron energy spectrum and wave function have been found by solving Schrodinger equation using the standard finite-difference method.

Analysis of Figure 34 reveals the effect of growing In concentration x in the nanogroove layer on the electron wave function (the built-in field $F_{\text{built-in}}$ is assumed to be 600 kV/cm). Due to the built-in field, in the conventional AlN/GaN/AlN QW the electron w.f. is squeezed to

one of the AlN/GaN interfaces. In QW with $\text{In}_x\text{Ga}_{1-x}\text{N}$ nanogroove, the increase in In content leads to the electron w.f. (and probability density) shift to the middle of QW, thus, among other things, reducing the electron-interface optical phonon interaction. For x changing from 0 to 0.02, the nanogroove depth increases but the energy difference $\Delta \varepsilon_{21} = \varepsilon_2^0 - \varepsilon_1^0$ between the ground (ε_1^0) and the first excited (ε_2^0) electron states reduces (see Table I). As x continues to grow, the $\Delta \varepsilon_{21}$ trend reverses since the electron w.f. becomes more localized; the shift closer to the QW center continues. For $x = 0.03$ the w.f. maximum is almost exactly in the middle of the well. The energy $\Delta \varepsilon_{21}$, the energy difference between ε_2^0 and the Fermi level ε_{F} for different x and two values of the built-in field $F_{\text{built-in}}$ are listed in Table I to elucidate the trends. The data is presented for the temperature $T = 300$ K and practically relevant electron concentration $N_{\text{s}} = 5 \cdot 10^{12} \text{ cm}^{-2}$ (degenerate electron gas).

The phonon engineering aspect of our analysis is electron interaction with the interface phonons at the nanogroove boundaries. The $\text{In}_x\text{Ga}_{1-x}\text{N}$ nanogroove has been introduced to push the electron w.f. away from the AlN/GaN interface, and tune the electron energy $\Delta \varepsilon_{21}$. From the other side, the introduction of an additional layer in the heterostructure results in additional IF phonon modes. By limiting ourselves to a certain In content range ($x \leq 0.06$) and tuning dimensions of the heterostructure we ensure that the potentials of the interface phonon modes at the GaN/ $\text{In}_x\text{Ga}_{1-x}\text{N}$ boundary are negligible. The square of the ratio of IF phonon potentials $\Gamma_{\text{S,A}}(z, q) = (V_{\text{S,A; IF}}^{\text{In}_x\text{Ga}_{1-x}\text{N}/\text{GaN}}(z, q)/V_{\text{S,A; IF}}^{\text{GaN}/\text{AlN}}(z, q))^2$ for In content $x = 0.07$ for small q and the lowest symmetric (S) and antisymmetric (A) IF modes is smaller than 0.03. As a result, the reduction of the electron mobility due to the introduction of additional $\text{In}_x\text{Ga}_{1-x}\text{N}/\text{GaN}$ interfaces is below 1% for $x = 0.07$.

The room-temperature electron mobility μ , calculated as a function of x , is shown in Figure 35 for three electron densities $N_{\text{s}} = 10^{11} \text{ cm}^{-2}$, $N_{\text{s}} = 10^{12} \text{ cm}^{-2}$ and $N_{\text{s}} = 5 \cdot 10^{12} \text{ cm}^{-2}$. The initial mobility reduction in the interval $0 < x \leq 0.02$ is explained by the enhanced inter-subband

Table I. Dependence of μ , $\varepsilon_2^0 - \varepsilon_{\text{F}}$, and $\Delta \varepsilon_{21}$ on F and x .

Built-in electric field (kV/cm)	x (In)	μ ($\times 10^3 \text{ cm}^2/\text{V s}$)	$(\varepsilon_2^0 - \varepsilon_{\text{F}})$ (meV)	$\Delta \varepsilon_{21}$ (meV)
$F = 600$	$x = 0.0$	3.54	98.8	154.9
	$x = 0.02$	3.39	48.46	101.8
	$x = 0.05$	16.5	123.3	181.8
	$x = 0.07$	14.5	176.9	236.5
	$x = 0.0$	3.26	159.8	216.8
$F = 1000$	$x = 0.02$	3.05	63.1	117.8
	$x = 0.05$	13	113.7	172
	$x = 0.07$	12.2	169.2	228.8

Source: Reprinted with permission from [22], E. P. Pokatilov et al., *Appl. Phys. Lett.* 89, 112110-1 (2006). © 2006, American Institute of Physics.

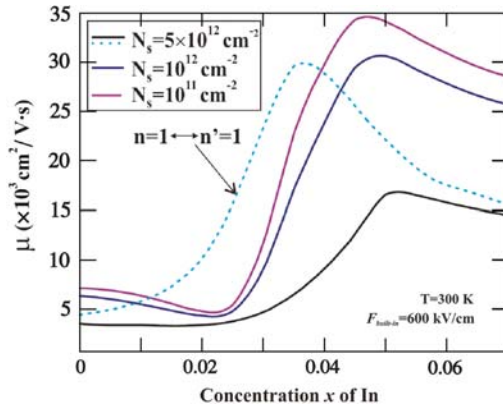


Fig. 35. Electron mobility as a function of In content x in the nanogroove. The results are shown for three electron concentrations: $N_s = 5 \cdot 10^{12} \text{ cm}^{-2}$ (solid), $N_s = 10^{12} \text{ cm}^{-2}$ (dashed), and $N_s = 10^{11} \text{ cm}^{-2}$ (dotted). Mobility calculated for the electron transitions within the first sub-band only is shown by the dash-dotted curve for $N_s = 5 \cdot 10^{12} \text{ cm}^{-2}$. Reprinted with permission from [22], E. P. Pokatilov et al., *Appl. Phys. Lett.* 89, 112110-1 (2006). © 2006, American Institute of Physics.

scattering due to the proximity of ε_2^0 and ε_F energy levels (see Table I). Further increase of In content in the $\text{In}_x\text{Ga}_{1-x}\text{N}$ nanogroove ($x \geq 0.04$) leads to a gradual suppression of the inter-subband transitions (via stronger w.f. localization), and weakens electron interaction with the AlN/GaN interface phonon modes owing to the w.f. shift to the QW center (see Fig. 34). At the same time, electron interaction with the confined optical phonons starts to grow due to the increase of the electron density in the middle of QW. The interplay of these trends results in achieving a maximum mobility for x in the range 0.045–0.055.

For $x \geq 0.055$, the mechanisms, which led to the mobility enhancement (weakening of the inter-subband transitions and suppression of the electron–interface optical phonon scattering) become less effective while increased localization of the electron w.f. results in growing strength of the electron interaction with confined optical phonons. The latter explains the mobility reduction for $x > 0.055$. In Figure 35, we also show the electron mobility (dash-dotted curve), which was calculated assuming the intra-subband ($1 \leftrightarrow 1$) scattering only, and by completely neglecting $1 \leftrightarrow 2$ and $2 \leftrightarrow 2$ scattering transactions. As one can see, this curve strongly differs from the mobility calculated with all relevant scattering mechanisms (solid curve). This confirms that in the considered heterostructures the inter-subband electron transitions play an important role.

In Figure 36 we plotted the mobility enhancement factor—ratio of the electron mobility in the $\text{AlN}/\text{GaN}/\text{AlN}$ QW with $\text{In}_x\text{Ga}_{1-x}\text{N}$ nanogroove to the electron mobility in the conventional $\text{AlN}/\text{GaN}/\text{AlN}$ QW. The ratio, defined as $R(x, T) = \mu(x, T)/\mu(x=0, T)$, is plotted as a function of In content x and temperature T for the electron concentration of $N_e = 5 \cdot 10^{12} \text{ cm}^{-2}$. The maximum enhancement R_{max} is in the range from four to five for all considered

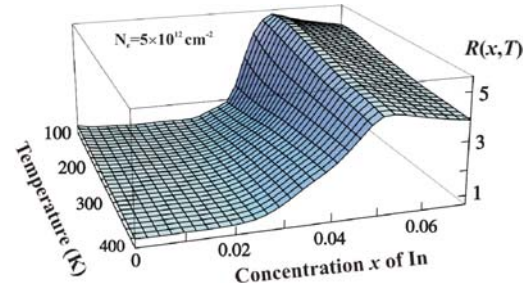


Fig. 36. Mobility enhancement factor as a function of temperature and In content x . Reprinted with permission from [22], E. P. Pokatilov et al., *Appl. Phys. Lett.* 89, 112110-1 (2006). © 2006, American Institute of Physics.

temperatures. The intriguing result is that μ enhancement is preserved at elevated $T \sim 400 \text{ K}$ and above, which is important for GaN-based high power-density devices.

A direct comparison of the calculated μ with experiment is currently not possible since the available data for AlGaIn/GaN HFETs is affected by the electron spillover, parallel conduction channels, defects, etc.^{59,60} It is meaningful though to validate the model using data reported for similar structures. Levinshtein et al.⁶¹ reported $\mu = 0.14 \text{ m}^2/\text{V s}$ for GaN-based HFETs with additional SiO_2 barrier layer for improved carrier confinement. Our calculated value for $N_s = 10^{13} \text{ cm}^{-2}$ and uncompensated 2000 kV/cm field is only 25% higher, which can be explained by the neglected surface roughness and defect scattering.

In conclusion, we have shown that the mobility in GaN-based QWs with the strong built-in field can be substantially enhanced by compensating the built-in field with the external perpendicular electric field or introduction of narrow $\text{In}_x\text{Ga}_{1-x}\text{N}$ channel-nanogroove in the middle of the GaN potential well. The enhancement is strong even at $T = 300 \text{ K}$ for a wide range of the carrier densities. The intriguing non-monotonic dependence of the mobility on electric field and Indium concentration is explained by the interplay of the intra- and inter-subband scattering processes. The described μ enhancement via introduction of $\text{In}_x\text{Ga}_{1-x}\text{N}$ nanogroove is expected to work in the presence of the structural defects as well. The outlined approach for the mobility enhancement at room temperature and above might be useful for optimization of layout of the GaN-based high-power transistors.

Acknowledgments: The work was supported in part through the U.S. Civil Research and Development Foundation (CRDF) project MOE2-3057-CS-03 and the state projects of the Republic of Moldova no. 06.408.036F and 06.35 CRF. One of the authors, A.A.B. also acknowledges the support from the National Science Foundation and MARCO Center on Functional Engineered Nano Architectonics (FENA).

References and Notes

1. J. M. Ziman, *Electrons and Phonons*, University Press, Oxford (1979).
2. A. A. Balandin, Plenary Talk: Acoustic Phonon Confinement in Nanostructures and Its Effect on the Thermal Conductivity, *Proceedings of the PHONONS 2004 International Conference*, Ioffe Institute, St. Petersburg, Russia (2004).
3. S. M. Rytov, *Akust. Zh. Akust. Zh. (USSR)* 2, 71 (1956); *Sov. Phys. Acoust.* 2, 67 (1956).
4. C. Colvard, T. A. Gant, M. V. Klein, R. Merlin, R. Fisher, H. Morkoc, and A. C. Gossard, *Phys. Rev. B* 31, 2080 (1985).
5. M. A. Strosio, K. W. Kim, SeGi Yu, and A. Ballato, *J. Appl. Phys.* 76, 4670 (1994).
6. N. Bannov, V. Mitin, and M. Strosio, *Phys. Stat. Sol. (b)* 183, 131 (1994).
7. N. Nishiguchi, Y. Ando, and M. Wybourne, *J. Phys. Condens. Matter.* 9, 5751 (1997).
8. A. Svizhenko, A. Balandin, S. Bandyopadhyay, and M. Strosio, *Phys. Rev. B* 57, 4687 (1998).
9. S. I. Borisenko, *Semiconductors* 38, 824 (2004).
10. A. A. Balandin and K. L. Wang, *Phys. Rev. B* 58, 1544 (1998).
11. J. Zou and A. Balandin, *J. Appl. Phys.* 89, 2932 (2001).
12. A. A. Balandin, *Phys. Low-Dim. Structures* 5–6, 73 (2000).
13. A. A. Balandin, D. L. Nika, and E. P. Pokatilov, *Phys. Stat. Sol. (c)* 1, 2658 (2004).
14. E. P. Pokatilov, D. L. Nika, and A. A. Balandin, *Superlatt. Microstruct.* 33, 155 (2003).
15. E. P. Pokatilov, D. L. Nika, and A. A. Balandin, *Phys. Rev. B* 72, 113311-1 (2005).
16. E. P. Pokatilov, D. L. Nika, and A. A. Balandin, *Superlatt. Microstruct.* 38, 168 (2005).
17. O. L. Lazarenkova and A. A. Balandin, *Phys. Rev. B* 66, 245319 (2002).
18. A. A. Balandin, *Phys. Low-Dim. Structures* 1–2, 1 (2000).
19. E. P. Pokatilov, D. L. Nika, and A. A. Balandin, *Appl. Phys. Lett.* 85, 825 (2004).
20. E. P. Pokatilov, D. L. Nika, and A. A. Balandin, *J. Appl. Phys.* 95, 5626 (2004).
21. E. P. Pokatilov, D. L. Nika, and A. A. Balandin, *Appl. Phys. Lett.* 89, 113508 (2006).
22. E. P. Pokatilov, D. L. Nika, and A. A. Balandin, *Appl. Phys. Lett.* 89, 112110 (2006).
23. A. A. Balandin and J. Zou, *Thermal Transport in Semiconductor Nanostructures*, Advances in Nanophase Materials and Nanotechnology, edited by S. Bandyopadhyay and H. S. Nalwa, American Scientific Publishers, Los Angeles (2003), pp. 303–336.
24. A. A. Balandin, (ed.), *Thermal Conductivity of Semiconductor Nanostructures*, in *Encyclopedia of Nanoscience and Nanotechnology*, American Scientific American Scientific Publishers, Los Angeles (2004), pp. 425–445.
25. D. Li, Y. Wu, P. Kim, L. Shi, P. Yang, and A. Majumdar, *Appl. Phys. Lett.* 83, 2934 (2003).
26. W. P. Meson, (ed.), *Physical Acoustic*, Academic Press, New York (1964), Vol. I, Part A.
27. N. Bannov, V. Aristov, V. Mitin, and M. A. Strosio, *Phys. Rev. B* 51, 9930 (1995).
28. O. Stier and D. Bimberg, *Phys. Rev. B* 55, 7726 (1997).
29. I. Vurgaftman, J. R. Meyer, and L. R. Ram-Mohan, *J. Appl. Phys.* 89, 5815 (2001).
30. V. Bougrov, M. Levinstein, S. L. Rumyantsev, and A. Zubrilov, *Properties of Advanced Semiconductor Materials*, edited by M. E. Levinstein, S. L. Rumyantsev, and M. S. Shur, J. Wiley & Sons, Inc., New York (2001).
31. See for example at https://classes.yale.edu/eeng418a/classnotes/EE418_c13.pdf.
32. See for example at <http://www.ondacorp.com/tables/Plastics.pdf>.
33. A. Bykhovski, B. Gelmont, and M. Shur, *J. Appl. Phys.* 74, 6734 (1993).
34. A. Bykhovski, B. Gelmont, and M. Shur, *J. Appl. Phys.* 78, 3691 (1995).
35. A. Bykhovski, B. Gelmont, and M. Shur, *J. Appl. Phys.* 81, 6332 (1997).
36. F. Bernardini, V. Fiorentini, and D. Vanderbilt, *Phys. Rev. B* 56, R10024 (1997).
37. F. Bernardini and V. Fiorentini, *Phys. Rev. B* 57, R9427 (1998).
38. N. Nishiguchi, *Physica E* 13, 1 (2000).
39. N. Suzuki and N. Iizuka, *J. Appl. Phys.* 38, L363 (1999).
40. S.-H. Park, D. Ahn, and Y.-T. Lee, *J. Appl. Phys.* 40, L941 (2001).
41. V. G. Grigoryan and D. G. Sedrakyan, *Akust. Zh. (USSR)* 29, 470 (1983).
42. L. D. Landau and E. M. Lifshits, *Theory of Elasticity*, Fizmatlit, Moscow (2001).
43. J. Singh, *Physics of Semiconductors and Their Heterostructures*, McGraw-Hill, New York (1993), p. 397.
44. J. T. Devreese, V. M. Fomin, and E. P. Pokatilov, *Handbook of Semiconductor Nanostructures and Nanodevices*, edited by A. A. Balandin and K. L. Wang, American Scientific Publishers, North Levis Way (2006), Vol 4, pp. 340–407.
45. B. K. Ridley, B. E. Foutz, and L. F. Eastman, *Phys. Rev. B* 61, 16862 (2000).
46. D. R. Anderson, N. A. Zakhleniuk, M. Babiker, B. K. Ridley, and C. R. Bennett, *Phys. Rev. B* 63, 245313 (2001).
47. B. C. Lee, K. W. Kim, M. A. Strosio, and M. Dutta, *Phys. Rev. B* 58, 4860 (1998).
48. S. M. Komirenko, K. W. Kim, M. A. Strosio, and M. Dutta, *Phys. Rev. B* 59, 5013 (1999).
49. D. Zanato, S. Gokden, N. Balkan, B. K. Ridley, and W. J. Schaff, *Sci. Technol.* 19, 427 (2004).
50. S. Gokden, *Phys. Stat. Sol. (a)* 200, 369 (2003).
51. V. Yu. Davydov, A. A. Klochikhin, R. P. Seisyan, V. V. Emtsev, S. V. Ivanov, F. Bechstedt, J. Furthmuller, H. Harima, A. V. Mudryi, J. Aderhold, O. Semchinova, and J. Graul, *Phys. Stat. Sol. (b)* 229, R1 (2002).
52. J. Wu, W. Walukiewicz, K. M. Yu, J. W. Ager III, E. E. Haller, H. Lu, W. J. Schaff, Y. Saito, and Y. Nanishi, *Appl. Phys. Lett.* 80, 3967 (2002).
53. T. Matsuoka, H. Okamoto, M. Nakao, H. Harima, and E. Kurimoto, *Appl. Phys. Lett.* 81, 1246 (2002).
54. V. A. Fonoberov and A. A. Balandin, *Nano Letters* 5, 1920 (2005).
55. V. A. Fonoberov and A. A. Balandin, *Nano Letters* 6, 2442 (2006).
56. C. Adelman, E. Sarigiannidou, D. Jalabert, Y. Hori, J.-L. Rouviere, D. Daudin, S. Fanget, C. Bru-Chevallier, T. Shibata, and M. Tanaka, *Appl. Phys. Lett.* 82, 4154 (2003).
57. S. Pereira, M. R. Correia, T. Monteiro, E. Pereira, E. Alves, A. D. Sequeira, and N. Franco, *Appl. Phys. Lett.* 78, 2137 (2001).
58. F. B. Naranjo, M. A. Sánchez-García, F. Calle, E. Calleja, B. Jenichen, and K. H. Ploog, *Appl. Phys. Lett.* 80, 231 (2002).
59. X. Z. Dang, P. M. Asbeck, E. T. Yu, G. J. Sullivan, M. Y. Chen, B. T. McDermott, K. S. Boutros, and J. M. Redwing, *Appl. Phys. Lett.* 74, 3890 (1999).
60. A. Balandin, S. Morozov, S. Cai, R. Li, K. L. Wang, G. Wijeratne, and C. R. Viswanathan, *IEEE Trans. Microwave Theory Microwave Theory Tech.* 47, 1413 (1999).
61. M. E. Levinstein, P. A. Ivanov, M. Asif Khan, G. Simin, J. Zhang, X. Hu, and J. Yang, *Semicond. Sci. Technol.* 18, 666 (2003).

Received: 10 January 2007. Revised/Accepted: 20 March 2007.